Combining CO_2 conversion and N_2 fixation in a gliding arc plasmatron

Reference:
Ramakers Marleen, Heijkers Stijn, Tytgat Tom, Lenaerts Silvia, Bogaerts Annemie.- Combining CO_2 conversion and N_2 fixation in a gliding arc plasmatron
Journal of CO2 utilization - ISSN 2212-9820 - 33(2019), p. 121-130
Full text (Publisher's DOI): https://doi.org/10.1016/J.JCOU.2019.05.015
To cite this reference: https://hdl.handle.net/10067/1599840151162165141

Combining CO_2 conversion and N_2 fixation in a gliding arc plasmatron

Marleen Ramakers[a], Stijn Heijkers[a], Tom Tytgat[b], Silvia Lenaerts[b] and Annemie Bogaerts[a]

[a] Research group PLASMANT, Department of Chemistry, University of Antwerp, Universiteitsplein 1, 2610 Antwerp, Belgium
[b] Research group DuEL, Department of Bioscience engineering, University of Antwerp, Groenenborgerlaan 171, 2020 Antwerp, Belgium

Abstract

Industry needs a flexible and efficient technology to convert CO_2 into useful products, which fits in the Carbon Capture and Utilization (CCU) philosophy. Plasma technology is intensively being investigated for this purpose. A promising candidate is the gliding arc plasmatron (GAP). Waste streams of CO_2 are often not pure and contain N_2 as important impurity. Therefore, in this paper we provide a detailed experimental and computational study of the combined CO_2 and N_2 conversion in a GAP. Is it possible to take advantage of the presence of N_2 in the mixture and to combine CO_2 conversion with N_2 fixation? Our experiments and simulations reveal that N_2 actively contributes to the process of CO_2 conversion, through its vibrational levels. In addition, NO and NO_2 are formed, with concentrations around 7000 ppm, which is slightly too low for valorization, but by improving the reactor design it must be possible to further increase their concentrations. Other NO-based molecules, in particular the strong greenhouse gas N_2O, are not formed in the GAP, which is an important result. We also compare our results with those obtained in other plasma reactors to clarify the differences in underlying plasma processes, and to demonstrate the superiority of the GAP.

Introduction

"A penny saved is a penny earned" is one important saying in industry. It is in this view that industry is looking for an easy and energy-efficient method to convert CO_2 from their waste streams. A technology intensively investigated for this purpose is based on plasma[1,2]. Plasma is created by applying electric power to a gas, causing breakdown of the gas into ions and electrons. It is thus a (partially) ionized gas, consisting of molecules, but also a large number of other species, such as various radicals, ions, excited species, and electrons. This makes plasma a highly reactive cocktail, useful for many applications[1,3]. The major advantage of plasma is that mainly the electrons are heated by the applied power, because of their small mass, and the energetic electrons can activate the gas by electron impact excitation, ionization, and dissociation, creating reactive species that can easily form new molecules. In this way, the gas as a whole does not have to be heated. Furthermore, owing to the fact that plasma can be switched on and off very easily, this technique also has great potential to store intermittent renewable energy, like solar and wind[2].
A very promising candidate for plasma-based CO_2 conversion is the gliding arc plasmatron (GAP). This is a three-dimensional gliding arc reactor[4,5]. A gliding arc (GA) plasma is created by applying a potential difference between two electrodes (cathode and anode), and typically moves (or glides) along these electrodes as a result of a gas flow. The GAP is a non-thermal plasma with different electron, and likely different vibrational, rotational and translational temperatures[6–8]. In the GAP under study here, the cathode forms the reactor body, while the reactor outlet is at anode potential.

The gas enters through 6 tangential inlets so that a vortex flow is obtained. This stabilizes the arc plasma in the center of the reactor and part of the gas flow is actually forced to go through the plasma, while only limited heat loss occurs to the reactor walls. Note that the plasma column is actually not just convected by the gas flow, but moves slower than the gas flow surrounding the plasma column[9,10]. The splitting of pure CO_2 and the dry reforming of methane (DRM) have already been investigated in this GAP[4,5,11], as well as in similar designs[12–20], and showed very promising results in terms of energy efficiency (i.e. up to 46 % for pure CO_2 splitting and up to 67 % for DRM). However, most industrial gas flows contain impurities, or even large gas admixtures, and it is often economically not feasible to separate them from the gas stream[21]. Aiming for the industrial implementation of this technology, it is crucial to study the effect of these impurities on the CO_2 conversion and on the formation of byproducts.

Most often, N_2 is the main compound in gas effluents[22]. Therefore, we study in this paper the effect of N_2 on the plasma chemistry of CO_2 conversion. We have performed experiments in a broad range of N_2 concentration to find out how it affects the CO_2 conversion, as well as the energy cost and energy efficiency. Furthermore, we analyzed which useful or harmful byproducts are formed. This is specifically interesting to find out whether purification is needed and whether pre- or post-purification steps would economically be most viable. Besides that, we also evaluate for the first time whether a mixture of CO_2 and N_2 could be a starting point for combined CO_2 conversion and N_2 fixation, i.e., the conversion of N_2 molecules into simple nitrogen compounds, that form the building blocks for life on Earth[23,24]. If sustainable electricity can be utilized for the plasma generation and further conversion of NOx into NH_3 can be realized, this can offer opportunities as a green alternative for the Haber-Bosch process[24,25] and more in general for N_2 fixation. It must be realized that the reaction products of the combined CO_2-N_2 conversion (CO and NOx) require separation or further oxidation steps to be used for fuel and fertilizer. Hence, this research is still on the fundamental level, and more research will be needed to bring it to real application. Finally, we have also performed chemical reaction simulations to unravel the underlying reaction pathways of CO_2 conversion in the presence of N_2, as well as of the byproduct formation.

To our knowledge, such a comprehensive experimental and computational study for the addition of N_2 to CO_2 in a GAP has never been performed. In addition, only a few papers have reported on the effect of N_2 on CO_2 conversion in other types of plasmas[16,26–28]. However, except in the paper by Snoeckx et al.[28], a detailed analysis of the byproduct formation in this mixture was never performed, which is of course crucial for practical applications. Furthermore, Snoeckx et al.[28] carried out this analysis for a dielectric barrier discharge (DBD), which has completely different plasma properties than a GAP[2]. The latter clearly affects the plasma chemistry, and thus the CO_2 conversion and byproduct formation. This will also be illustrated in this paper.

Description of the experiments

Gliding arc setup

The experiments were performed with a gliding arc plasmatron (GAP), which was developed at Drexel University by Nunnally et al.[4] and was previously described in detail[5]. A schematic picture of the GAP is shown in Figure 1. The cathode (reactor body) has a length of 10.20 mm and a diameter of 17.50 mm, while the anode has a length of 16.30 mm and a diameter of 7.08 mm. These dimensions give rise to a reactor volume of 6.22 cm^3, but the arc volume is only about 0.13 cm^3. Indeed, it takes place only in the center of the reactor, thereby isolating the reactor walls from the hot plasma. A photograph and diagram of the entire experimental system is shown in Figure 2.

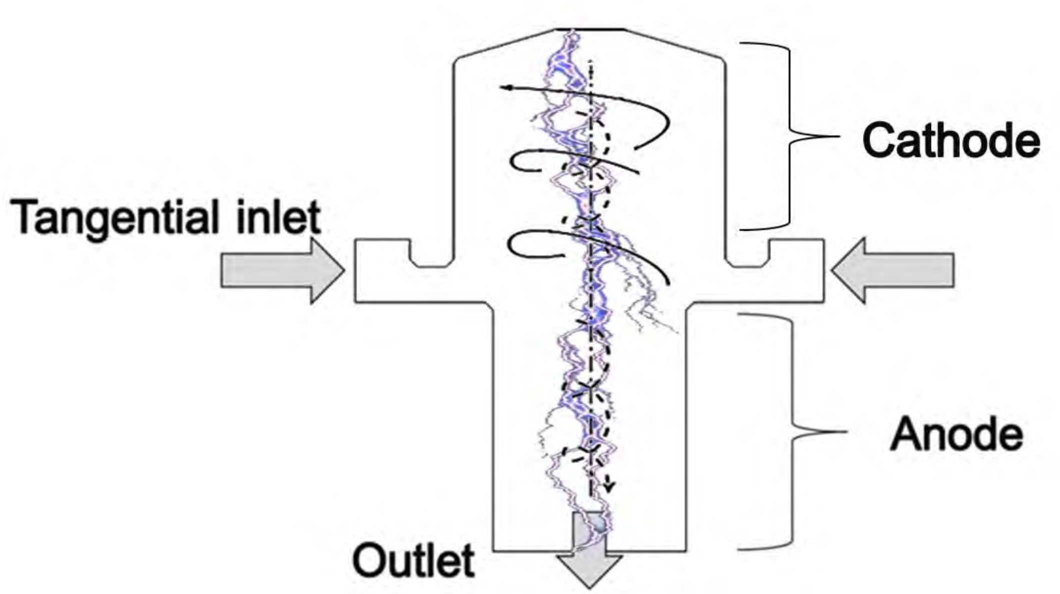

Figure 1. Schematic picture of the gliding arc plasmatron in reverse vortex flow configuration. Both the forward and reverse vortex flows are indicated (with full and dashed spirals, respectively). This vortex flow configuration stabilizes the arc discharge (indicated in purple) in the center of the reactor and forces the reverse gas flow to go through the plasma.

Mass Flow Controllers (Bronkhorst) were used to insert CO_2 and N_2 into the GAP. The total flow rate was kept constant at 10 L/min. The N_2 concentration was varied between 5 and 95 %. The reactor was powered by a DC current source type power supply. The plasma voltage and current were measured by a high-voltage probe (Tektronix P6015A) and a current sense resistor of 6 Ω, respectively. The electrical signals were sampled by a two-channel digital storage oscilloscope (Tektronix TDS2012C). The current was set at 0.23 A. The plasma power was calculated as the product of the plasma voltage and current over a certain time. All the experiments were performed three times. Subsequently, a propagation of uncertainty was applied to the results, to calculate the error bars.

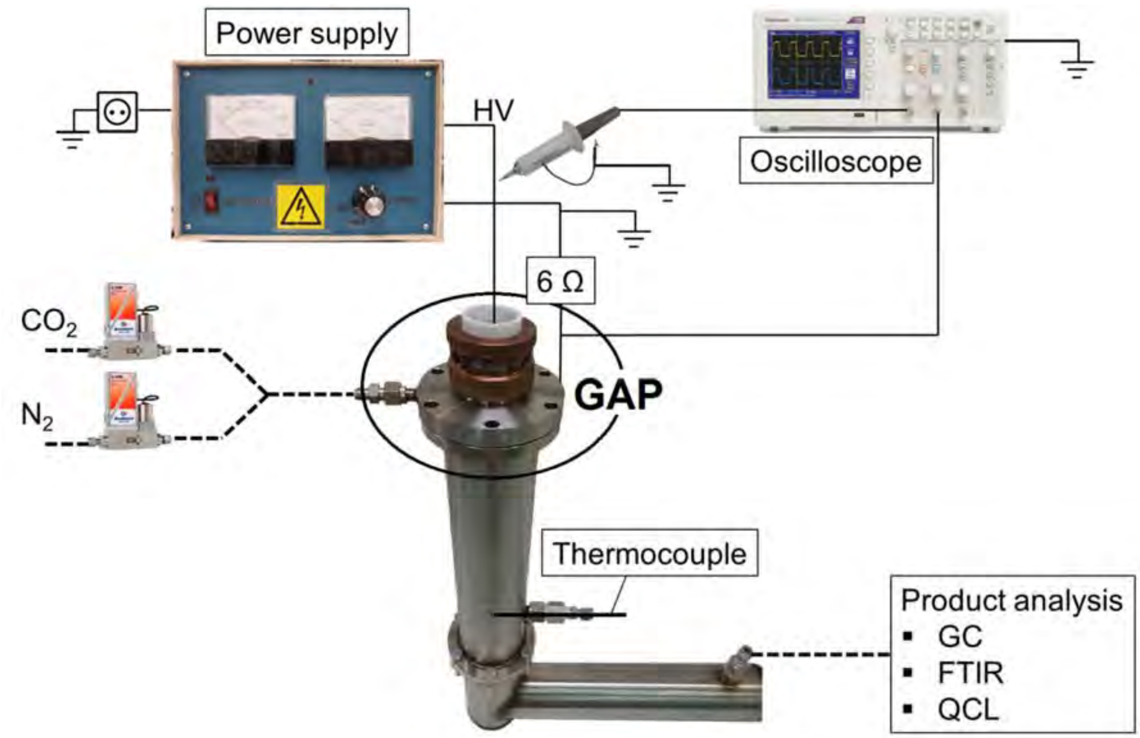

Figure 2. The plasma in the gliding arc plasmatron (GAP) is initiated by applying a high voltage over two electrodes with a power supply. The setup is completed by Mass Flow Controllers for gas input and measuring equipment, i.e., electrical (oscilloscope), temperature (thermocouple) and product analysis.

Product analysis

The output gas composition is analyzed with three different gas analysis techniques: gas chromatography (GC)[5], Fourier Transform Infrared spectroscopy (FTIR)[28] and Quantum Cascade Laser (QCL) technology. The feed and main product gases (CO_2, N_2, CO, O_2) were analyzed by a three-channel compact gas chromatograph (CGC) from Interscience. Besides CO and O_2, some other products, like O_3 and NOx compounds (i.e., NO, NO_2, N_2O, N_2O_3 and N_2O_5) can be formed. We used a Nicolet 380 Fourier-Transform Infrared (FTIR) spectrometer (Thermo Fischer Scientific, Waltham, MA) and a CT5800 Analyzer (Emerson, Stirling, UK) based on Quantum Cascade Laser (QCL) technology to qualitatively and quantitatively analyze these products, respectively. These techniques, as well as the associated formulas to calculate the conversion, energy cost and energy efficiency, are described in detail in the Supplementary Information (Suppl. Info.).

Description of the model

The model used to simulate the chemical reactions in the GAP, is a 0D chemical kinetics model. It solves a set of conservation equations (Equation 1) for all individual species included in the model:

$$\frac{dn_i}{dt} = \sum_j [(a_{ij}^R - a_{ij}^L) k_j \prod_{lj} n_{lj}] \quad (1)$$

n_i is the density of species i, a_{ij}^R and a_{ij}^L are the stoichiometric coefficients of the species i on the right and left hand side of the reaction *j*, respectively, n_{lj} is the density of the species l on the left side of reaction *j*, and k_j is the reaction rate coefficient of reaction *j*. For example, for the jth reaction A + B → C + D, the conservation equation for the density of species B is $\frac{dn_B}{dt} = (0-1)k_j n_A n_B$.

An extensive chemistry set, containing 18180 reactions and 134 species, is included in the model. The species interact with each other through electron impact reactions, electron-ion recombination, ion-ion, ion-neutral and neutral-neutral reactions, as well as vibration-translation (VT) and vibration-vibration (VV) relaxation. More information on these reactions and the list of species, as well as more details on the model, can be found in the Suppl. Info., including the GAP geometry as treated in the 0D model (Figure S1).

Results and discussion

<u>CO_2 conversion, energy cost and energy efficiency</u>

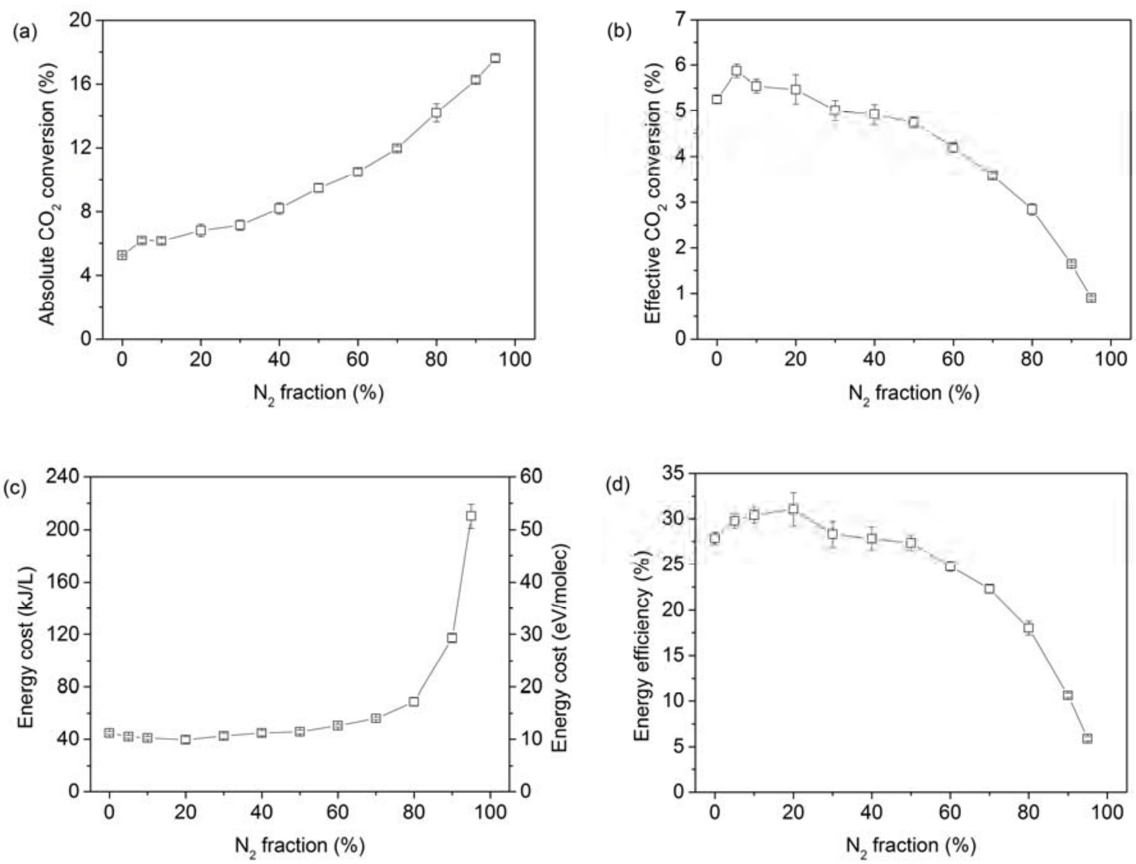

Figure 3. Absolute (a) and effective (b) CO_2 conversion, energy cost (c) and energy efficiency (d), as a function of N_2 fraction, at a total flow rate of 10 L/min and a plasma power of 350 W. The error bars are included in the graphs, but are sometimes too small to be visible.

Figure 3(a) shows that the absolute CO_2 conversion rises from 5 to 18 % with increasing fraction of N_2 in the mixture. Hence, N_2 helps to convert CO_2, by the transfer of vibrational energy, as explained in section 'Simulation results' below. Indeed, CO_2 conversion in a GAP is most effective through the vibrational levels[5,29], and the N_2 vibrational levels help to populate these CO_2 vibrational levels. The same mechanism was also found for a microwave (MW) plasma[26], while in a DBD plasma, another mechanism is more prominent, i.e., energy transfer from the electronically excited N_2 molecules[28].
The effective CO_2 conversion is obtained by accounting for the initial fraction of CO_2 in the mixture (see Equation (2) in the Suppl. Info.). Until a N_2 fraction of 50 %, the effective conversion only slightly

decreases, while above 50 %, the effective conversion drops quite fast from 5 to 1 % (see Figure 3(b)). Thus, at N_2 fractions below 50 %, the increase in absolute CO_2 conversion can more or less compensate for the lower CO_2 concentration in the mixture, but at higher N_2 fractions, this is not true anymore. Indeed, not all the energy of the vibrationally excited N_2 is transferred into CO_2 dissociation, and part of it also remains stored in the N_2 vibrational levels or gets lost by collisions with ground state molecules (so-called VT relaxation). Thus, at higher N_2 fractions in the mixture, a larger portion of the applied power is used to activate the N_2 molecules, without converting all this energy into CO_2 dissociation.
The energy cost of CO_2 conversion is calculated with equation (4) in the Suppl. Info., and is shown in Figure 3(c). Until a N_2 fraction of 70 %, the energy cost is about 40 kJ/L (or 10 eV/molec). At higher N_2 fractions, it rises dramatically to 210 kJ/L (or 52.5 eV/molec). The energy efficiency of CO_2 conversion (see Figure 3(d)) more or less follows the trend of the effective CO_2 conversion, since it is approximately proportional to it. The fact that it does not exhibit exactly the same trend is due to a small drop in specific energy input (SEI) upon N_2 addition (see Figure S3 in the Suppl. Info.), as the energy efficiency is inversely proportional to the SEI (see equation (5) in the Suppl. Info.). The energy efficiency remains more or less constant around 28 % until 50 % N_2, after which it decreases rapidly to a value of 5 %. Thus, upon increasing N_2 fraction, more energy is consumed by the N_2 molecules, which cannot be used anymore for CO_2 conversion. We can thus conclude that up to 50 %, N_2 has little effect on the effective (i.e., overall) CO_2 conversion, its energy cost and energy efficiency. In this respect, there is no need to separate N_2 from CO_2 in waste streams containing at maximum 50 % N_2.

The energy cost and energy efficiency reached in our GAP are very good compared to other plasma reactors, i.e., DBD and MW plasma[26,28]. This is clearly demonstrated from Figure S4 in the Suppl. Info., where the energy efficiency is plotted against CO_2 conversion in GAP, DBD and MW plasma. The best energy efficiency is reached in our GAP, but for the CO_2 conversion, there is still room for improvement, and the MW plasma reaches higher conversion. Nevertheless, the experiments with MW plasma were performed at reduced pressure (2660 Pa), while the GAP and DBD both operate at atmospheric pressure. If the pressure in the MW plasma would be increased, the conversion and energy efficiency would drop[2,30,31], and in addition the plasma would become less stable[2,31]. When operating at reduced pressure, the energy cost of pumping should also be accounted for, and this would lower the overall energy efficiency (not yet included in Figure S4). For industrial application of this technology, it would be beneficial to work at atmospheric pressure or higher.

<u>Analysis of the byproducts - NOx concentrations</u>

Not only conversion and energy efficiency are important for evaluation of this technology, but also the formation of byproducts. We used FTIR as qualitative analysis method for the byproducts, i.e., O_3 and NOx compounds (NO, NO_2, N_2O, N_2O_3 and N_2O_5). Note that in terms of N_2 fixation, the NOx compounds are products rather than byproducts. However, as the main goal of the research was CO_2 conversion (in the presence of N_2 from a waste stream), the NOx compounds can be considered as byproducts, which can be of added value as well, if produced in sufficient amounts. The components that could be clearly distinguished from the FTIR-spectrum are CO, NO and NO_2. There were no signals visible for other components, like O_3, N_2O, N_2O_3 and N_2O_5. The influence of N_2 fraction on the NO and NO_2 concentration in arbitrary units is plotted in Figure S5 of the Suppl. Info. To quantitatively analyze the NOx compounds, we used a CT5800 Analyzer based on Quantum Cascade Laser (QCL) technology. The QCL could not detect any N_2O, in agreement with the FTIR analysis, indicating that the concentration of N_2O was never higher than 1 ppm. The concentrations of NO and NO_2 as well as the sum of both, are plotted in Figure 4 as a function of N_2 fraction. The error bars are too small to be visible, as they were typically below 1 % of the actual concentrations, but the actual values of the concentrations, along with their absolute errors, are listed in Table S4 of the Suppl. Info. All curves show a maximum around 50 - 70 % N_2. This is expected, because in this range, both CO_2 and N_2 split into the reactive species needed for NO and NO_2 formation. At very low or high N_2 fractions, either N_2 or CO_2 will act as limiting reactant. The fact that the maximum NO concentration is reached around 60-70% N_2 indicates that CO_2 dissociation occurs easier than N_2 dissociation, which is explained by the C=O vs N≡N bond dissociation energy (i.e., 749 kJ/mol vs 946 kJ/mol). The maximum NO_2 concentration is reached at 50 % N_2, which is lower than for the maximum NO concentration. This is expected, because more CO_2 is needed, and thus less N_2, for the further oxidation of NO to NO_2 (see Figure 6). Looking at the absolute values, the NO concentration is about 20 times higher than for NO_2, with maximum values of 6453 and 317 ppm, respectively.

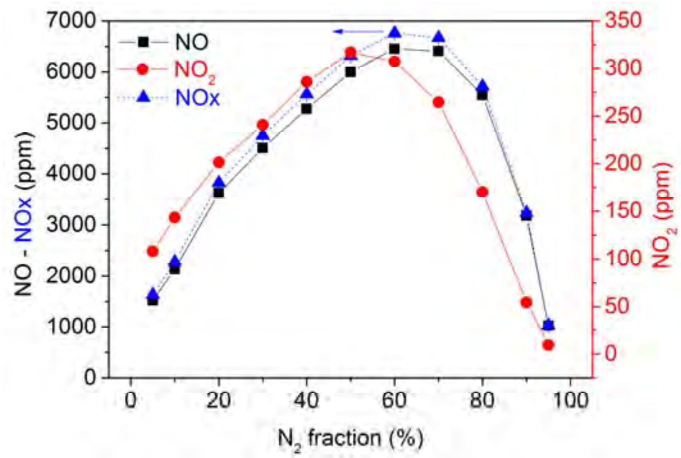

Figure 4. NO (left axis), NO_2 (right axis) and total NOx (left axis) concentration as a function of N_2 fraction. The error bars are too small to be visible, as they were typically below 1 % of the actual concentrations.

The highest total NOx concentration is 6761 ppm, reached at 60 % N_2. Patil et al. reported the highest NOx formation in a pulsed power milli-scale classical (planar) gliding arc (GA) reactor[32,33] to be 2 %, with 9470 ppm NO and 10653 ppm NO_2 at 1 L/min and a 1/1 N_2/O_2 ratio. NO_2 formation from dry air in a classical GA was investigated by Bo et al.[34] in the context of VOC decomposition, reaching a maximum NO_2 content of 6982 ppm. Compared to our reactor, the NO_2 concentration lies much higher in the abovementioned studies. The reason is the higher temperature in our GAP, which favors NO above NO_2 formation, as revealed by our computer simulations. Moreover, these studies were for NOx formation from N_2/O_2 as a starting mixture, where simply more O_2 is available to form NO_2, while in our case it depends on the CO_2 conversion. Indeed, we investigate the possibilities for NOx formation from CO_2/N_2 as starting mixture. If this is feasible, we do not only fixate N_2 but also convert CO_2 at the same time. In this way we accomplish two goals at once.

A possible downside, however, can be the more complicated separation of CO from the mixture, compared to pure CO_2 splitting. Nevertheless, some technologies are already available today for the purification of CO-containing streams with emphasis on CO/N_2 separation, such as cryogenic distillation and absorption[35]. However, the associated energy consumption of such an approach and/or the poor stability of the absorbents have led researchers to concentrate on adsorption technologies, which are currently under development. Examples of adsorbents are zeolites (particularly Zeolites X and Y), modified activated carbons (particularly via impregnation with copper), as well as metal-organic frameworks[35]. In another approach, the produced NOx could be catalytically converted into HNO_3 first. Subsequently, the CO can be separated in a similar way by for example pressure swing adsorption (PSA) as in the case of pure CO_2 splitting. Hence, for this approach, the catalytic conversion of NOx into HNO_3 represents an extra step for the separation. This should be taken into account when investigating the economic feasibility of the combined CO_2/N_2 conversion. However, this is outside the scope of the present study.

Plasma-based NOx formation from N_2/O_2 mixtures has also been studied in a large number of other plasma types[32,33,36–49]. An overview of the measured values for NOx yield and energy consumption is given in Table 1. Note that only in our work and that of Snoeckx et al.[28] the starting mixture is CO_2/N_2, whereas in all other cases it is N_2/O_2.

Table 1. Overview of measured values for NOx yield and energy consumption for various plasma types[a].

plasma type	NOx concentration	energy consumption	ref
gliding arc plasmatron (GAP) (*)	0.7 % NOx	7.02 MJ/mol NOx	this work
DBD (*)	0.06 % NOx	442 MJ/mol NOx	28
DBD with γ-Al_2O_3 catalyst	0.5 % NOx	18 MJ/mol NOx	32,42
milliscale GA with pulsed power	2 % NOx	7.2 MJ/mol NOx	32,33
milliscale GA with pulsed power	0.8 % NOx	2.8 MJ/mol NOx	32,33
pulsed arc discharge	–	10.6 MJ/mol NOx	36
plasma arc jet	6.5 % NO	4.0 MJ/mol NO	37
laser-produced plasma	–	8.96 MJ/mol NO	38
exploding water jet discharge	1 % NOx	47.2 MJ/mol NOx	39
negative pulsed corona discharge	–	1638 MJ/mol NOx	40
positive pulsed corona discharge	–	1060 MJ/mol NOx	40
spark discharge	–	20.2 MJ/mol NOx	40
spark discharge	1 % NOx	2.41 MJ/mol NOx	41
MW discharge with MoO_3 catalyst	6 % NO	0.84 MJ/mol NO	43
pulsed MW discharge	6 % NO	0.60 MJ/mol NO	44
MW discharge with magnetic field	14 % NO	0.30 MJ/mol NO	45
MW discharge	0.6 % NOx	4.05 MJ/mol NOx	46
shielded sliding discharge	0.1 % NOx	15.4 MJ/mol NOx	47
electric arc (original Birkeland-Eyde process)	1 – 2 % NO	2.41 MJ/mol NO	48
electric arc with water injection	4.7 % NO	3.50 MJ/mol NO	49

[a]In some references, the NOx yield was not mentioned, and only the energy consumption was mentioned.
(*) CO_2/N_2 as starting mixture.

The NOx yield reported in literature ranges from 0.06 to 14 %, while the energy consumption ranges from 0.3 to 1638 MJ/mol NOx. Thus, the GAP seems to perform at the lower limit for the NOx yield, but it performs quite well in terms of energy consumption, with a moderate value around 7 MJ/mol

NOx. To make a fair comparison, however, we have to take into account that our starting mixture is CO_2/N_2. Therefore, the NOx yield is limited by the CO_2 conversion, which supplies the oxygen for NOx formation. In addition, this also affects the energy consumption, since part of the energy input is also used for CO_2 conversion and not only for NOx production. The real energy consumption for NOx formation in the GAP will thus be lower than 7 MJ/mol NOx.

For a DBD reactor with[32,42] and without catalyst[28], the NOx yield is lower with considerably higher energy consumption than for microwave (MW) and gliding arc (GA) discharges (although the energy consumption of 442 MJ/mol NOx from ref. [28] is again obtained for a CO_2/N_2 mixture, explaining the higher value). The reason is that MW and GA plasmas are characterized by a reduced electric field (i.e., ratio of electric field over gas number density) between 5 and 100 Td, where the dominant electron-induced process is vibrational excitation of N_2, [24] similar as for CO_2.[2] Thus, in GA and MW discharges large amounts of vibrationally excited N_2 molecules are present, which provide more energy-efficient N_2 dissociation. DBDs are characterized by higher reduced electric fields, above 100 – 200 Td, where mostly electronically excited species are involved in NOx production, which is thus limited by the higher energy cost for the formation of these species (see more details below).

Comparing our results with those of the milliscale GA from Patil et al.[32,33], their NOx yield is more than twice as high, while the energy consumption is quite similar. However, we produce NOx from CO_2/N_2 instead of N_2/O_2, and part of the energy is consumed by CO_2, as explained above. We can conclude that NOx production from a CO_2/N_2 mixture in a GAP is worth investigating further, since it has similar energy consumption than starting from an N_2/O_2 mixture and it can solve two problems at the same time. Some ways to increase the NOx yield in our GAP are suggested below.

The best results up to now were obtained in MW plasmas[43–45] but only at reduced pressure, which requires pumping, making it less attractive for industrial implementation, and it should be accounted for in the calculation of the energy consumption, which was not the case for the values in Table 1. Unfortunately, the cost for pumping was not mentioned in these references, so we cannot make a fair comparison between these and our data, which were obtained at atmospheric pressure.

To make the process effective for N_2 fixation, the NOx concentration should increase to about 1 %[23,50]. Indeed, such low concentrations can already provide high concentrations of HNO_3 [50]. The CO_2 conversion in our GAP is limited to 8 – 18 %, due to the limited amount of gas passing through the actual arc plasma[5,11,51]. If this fraction can be enhanced by optimizing the reactor design or the gas inlet system, it would yield higher CO_2 conversions, and thus the NOx concentration could also rise further. Previously we found that lowering the flow rate also increases the CO_2 conversion[5]. However, a minimum flow rate of 10 L/min is necessary for obtaining a stable plasma, because of the need of a good vortex flow pattern. Such a calculated vortex flow pattern was presented in the SI (Figure 6) of reference 5. From previous calculations we know that the fraction of gas passing through the arc is 15 %[11], meaning that the conversion inside the arc is about 71 %. Hence, we have to increase the fraction of gas passing through the arc up to minimum 22 %, which results in a CO_2 conversion of 16 %, if we want to reach a NOx concentration above 1 % (see more details in the Suppl. Info.). A way to increase this fraction is by decreasing the radius of one or more tangential inlets in order to create a higher flow velocity so that more gas is forced into the central vortex. Besides this approach, we also want to change the cathode design to increase the electric field, which also increases the plasma production and arc stability. Dedicated fluid dynamics simulations are needed to evaluate these approaches, which is the subject of our future work.

The selectivity towards NO and NO_2 (see Equation (2) and (3)) are plotted as a function of N_2 fraction in Figure 5.

$$NO\ selectivity\ (\%) = \frac{NO\ concentration}{concentration\ of\ (NO + NO_2)} \times 100\ \% \quad (2)$$

$$NO_2\ selectivity\ (\%) = \frac{NO_2\ concentration}{concentration\ of\ (NO + NO_2)} \times 100\ \% \quad (3)$$

The NO selectivity rises from 93 to 99 % with increasing N_2 fraction, while the NO_2 selectivity decreases from 7 to 1 %. These trends are similar as in Wang et al.[24] for NOx formation from a N_2/O_2 mixture in a milli-scale classical (planar) GA, but the absolute values are clearly different. Indeed, Wang et al.[24] obtained more or less equal selectivities of 50 % for NO and NO_2, except at very high or low N_2 concentrations, while in our GAP the selectivity towards NO is much higher than towards NO_2. This is attributed to the much higher temperature in our GAP (i.e., nearly 3000 K[51], vs. 1000 – 1500 K in the classical GA[24]), favoring NO above NO_2, as well as the different starting mixture, and hence different reaction mechanisms for the formation of NO and NO_2, as explained in the 'Simulation results' section.

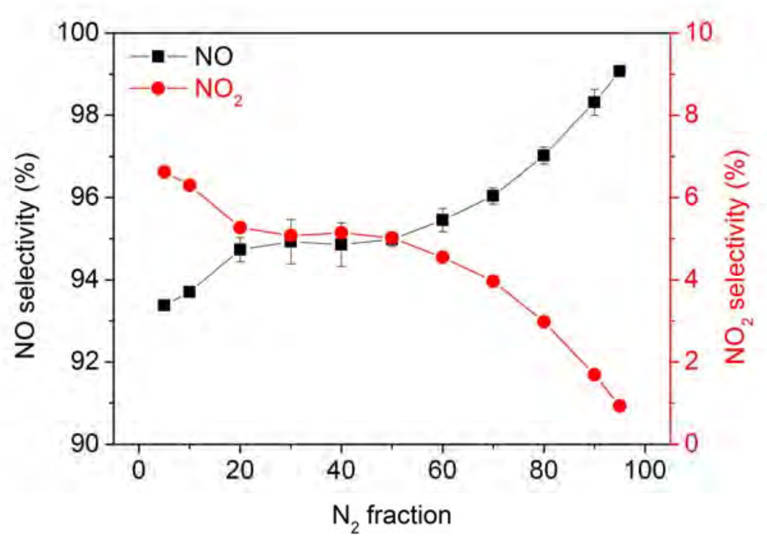

Figure 5. NO (left axis) and NO_2 (right axis) selectivity as a function of N_2 fraction. The error bars are included in the graph, but for some conditions they are too small to be visible.

In fact, the separate NO and NO_2 concentrations are not so important, as NO can easily be oxidized into NO_2 after plasma, so it is the total NOx concentration that counts. When the NOx concentrations will still be a bit higher and thus effective for N_2 fixation, the NO/NO_2 mixture can be separated from the unconverted fraction by taking part in the Ostwald process, thereby producing nitric acid[50]. This can be used as precursor for the synthesis of more complex molecules, such as mineral fertilizers. In the industrial Ostwald process, NH_3 is first oxidized to NOx and then absorbed by H_2O to form HNO_3. The typical yield from NH_3 to NOx is about 98 %. In our case, HNO_3 would also be made from NOx absorption by H_2O, but the yield from N_2 to NOx is considerably lower than in the industrial Ostwald process, so our process is by far not yet competitive with the Ostwald process. However, overall, producing HNO_3 from NH_3 is less sustainable, because the production of NH_3 is enormously energy intensive and produces a lot of CO_2. Hence, alternatives for the Haber-Bosch (HB) process must be investigated, and plasma technology is very promising in this respect, exactly because it can easily be combined with renewable energy, and it is thus a sustainable alternative, especially for distributed production. Furthermore, the energy efficiency is very good, due to the selective vibrational activation of the molecules. The potential of plasma technology was also recognized in a recent paper: "Nearly all nitric acid is manufactured by oxidation of NH_3 through the Ostwald process, but a more direct reaction of N_2 with O_2 might be practically feasible through further development of nonthermal plasma technology"[52].

Although several green technologies for NH_3 production from N_2 are being developed to replace the energy-intensive HB process[53–57], the goal of our plasma process is different: it is mainly used for CO_2 conversion, and by making use of a waste stream containing N_2, we can also produce NOx, which can be further converted to HNO_3, without producing NH_3 as an intermediate step. Hence, we believe our plasma process is a unique concept.

Underlying mechanisms as revealed by numerical simulations

We developed a chemical kinetics model to investigate the mechanisms of the combined CO_2 and N_2 conversion in our GAP (see brief explanation above and more details in the Suppl. Info.). The model has been validated against the experimental data for conversion, energy efficiency and NOx concentrations. In all cases, the trends and absolute values predicted by the model were in reasonable agreement with the experimental results, as illustrated in Figures S6 and S7 in the Suppl. Info. Indeed, on average the relative difference between calculated and experimental data was 5 % for the CO_2 conversion, 27 % for the N_2 conversion, 5 % for the energy efficiency, 34 % for the NO concentration, and 72 % for the NO_2 concentration. The largest deviation was found for NO_2 concentration, but keeping in mind the complexity of the underlying chemistry, this is still reasonable. Therefore, we can use the model to predict the underlying mechanisms. In Figures S8, S10 and S12 in the Suppl. Info., we present the net time-integrated rates of the most important reactions for the loss and formation of CO_2, NO and NO_2, respectively. For additional insight, we also plotted the net contributions of these reactions in Figures S9, S11 and S13 in the Suppl. Info.

For pure CO_2 the most important loss mechanism is the reaction of vibrationally excited CO_2 with O atoms, see Figure S8(a). This agrees well with earlier model predictions[5]. However, as soon as N_2 is added, the reaction of vibrationally excited CO_2 with NO becomes dominant, with an overall contribution of 50 – 60 % (Figure S9). Other reactions, such as the collision of vibrationally excited CO_2 with CN or any molecule M in the plasma, and electron impact dissociation of both CO_2 ground state and vibrationally excited levels, also play a role, with contributions of 5 – 60 %, depending on the N_2 fraction (Figure S9). CO_2 formation is mainly caused by recombination of CO and O_2 (Figure S8(b)), with contributions up to 80% (Figure S9). To prevent this recombination and thus enhance the CO_2 dissociation, we could separate O_2 from the mixture, e.g., by membrane technology or oxygen scavengers.

NO is initially formed upon reaction of vibrationally excited N_2 with O atoms, i.e., the so-called Zeldovich mechanism, in agreement with the dominant formation mechanisms in a milli-scale classical GA[24]. Subsequently, NO reacts with vibrational excited CO_2, forming CO and NO_2 (Figure S10). In return, the reaction of NO_2 with O atoms will further produce NO.

We summarize the most important reaction pathways in Figure 6. Reactants are indicated in color according to the time-integrated rate of their reaction (red ≥ 10^{17} cm^{-3}; green ≥ 10^{16} cm^{-3}; blue ≥ 10^{15} cm^{-3}), while the thickness of the arrow lines corresponds to the overall importance of the reaction. The most important reactions, ranked by importance based on the average time-integrated rates, are listed in Table S5 in the Suppl. Info.

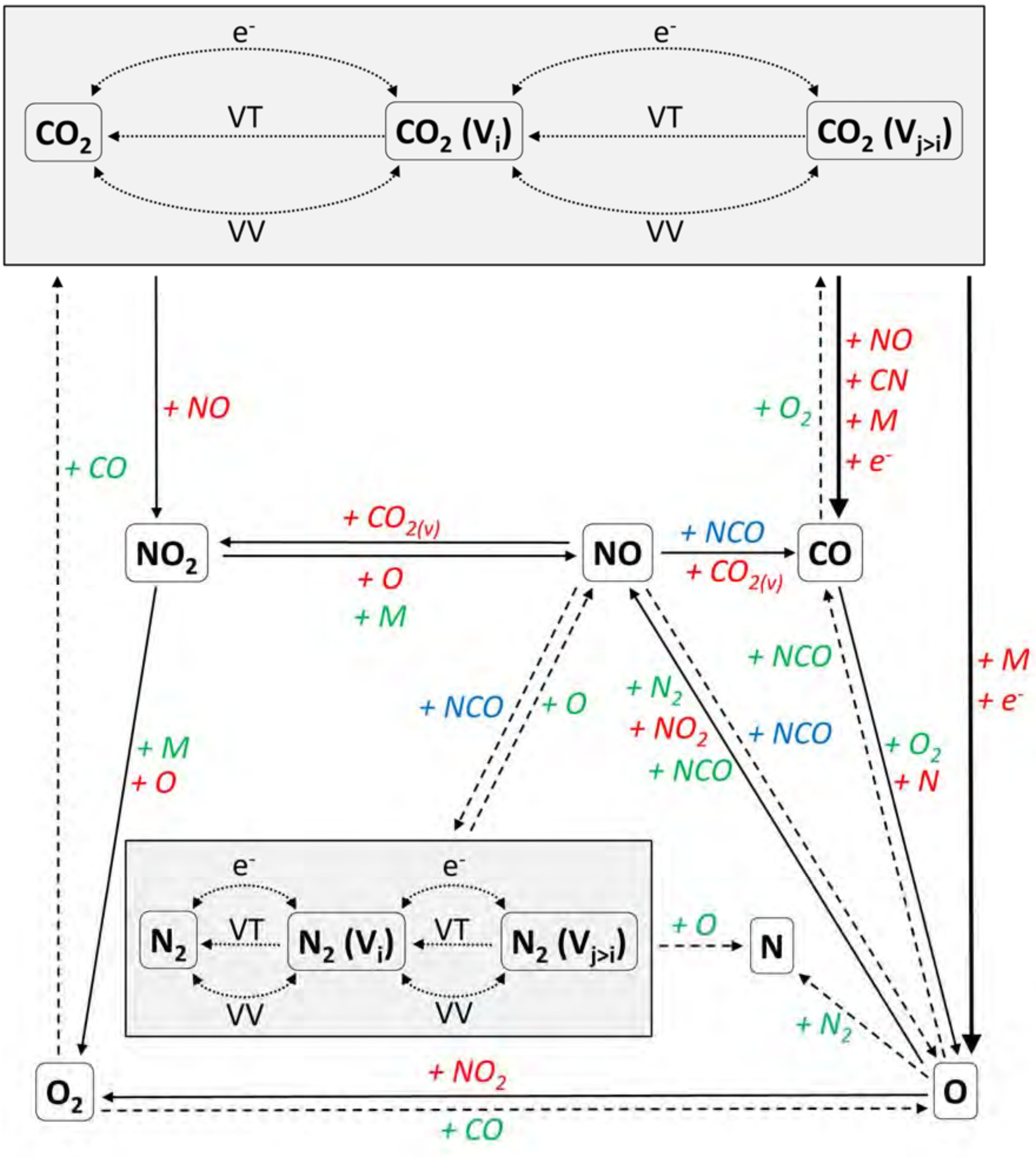

Figure 6. Reaction pathways for the conversion of CO_2 and N_2 into CO, O, O_2, N, NO and NO_2, as predicted by the model. Both CO_2 and N_2 are easily excited from ground state to vibrational levels and vice versa (dotted lines). The color of the reactants indicates the time-integrated rate of their reaction (red ≥ 10^{17} cm^{-3}; green ≥ 10^{16} cm^{-3}; blue ≥ 10^{15} cm^{-3}) while the thickness of the arrow lines corresponds to the total importance of the reactions (---< ——<

Both CO_2 and N_2 are easily excited from ground state to vibrational levels, and vice versa, upon electron impact (de)excitation, vibration-vibration (VV) and vibration-translation (VT) relaxation. The vibrational distribution functions (VDFs) of both CO_2 and N_2 are plotted in Figure S14. Overall, the VDF of both molecules is thermal, with a vibrational temperature of 3174 K and 3333 K for CO_2 and N_2, respectively (Figure S15), which is more or less equal to the gas temperature (3140 K). We should be able to increase the energy efficiency of CO_2 conversion and N_2 fixation if the VDFs of both CO_2 and N_2 would be more non-thermal, with higher populations of the higher vibrational level[5,29]. To realize this, the temperature in the arc should be reduced, so that VT relaxation, which depopulates the vibrational levels, can be reduced. On the other hand, the vibrational levels in our GAP are clearly more populated than in other types of plasmas, such as a DBD, where the VDF dramatically drops for the higher vibrational levels[58–60]. This explains why the CO_2 conversion and N_2 fixation are quite energy efficient, compared to other commonly studied plasma types (see Figure S4 in the Suppl. Info. and Table 1 above).

CO_2 is mainly converted into CO and O (right arrows in the figure), and it also helps in producing NO_2 upon reaction with NO. CO is in turn mainly converted into O by reaction with N or O_2. The N_2 molecules are activated by electron impact vibrational excitation (see Figure 6), lowering their energy barriers for chemical reaction with O atoms into NO formation. NO reacts further into NO_2, mainly by reaction with vibrationally excited CO_2. Vice versa, NO_2 also stimulates the formation of NO, by reaction with O atoms or any molecule (M) in the plasma. The fact that the most important loss mechanism of NO_2 is the most important formation mechanism of NO, and vice versa (Figure S10 and S12), shows that they are easily converted into each other. Still, the selectivity of NO is much higher in our GAP than that of NO_2. Indeed, NO is also formed upon reaction of O atoms with vibrationally excited N_2 (Zeldovich mechanism; cf. above) and with NCO, which have no reverse reaction (Figure S10). Thus, by comparing the sum of the time-integrated formation and loss rates, the resulting concentration of NO is 20 times higher than that of NO_2 (see Figure 5), which explains the higher NO selectivity.

We can in general conclude from Figure 6 that the NOx molecules are mainly formed through reactions with O atoms. So to enhance the NOx production, we have to stimulate the formation of O atoms, and thus the CO_2 conversion, e.g., by improving the reactor design to enhance the fraction of gas passing through the arc.

Finally, as mentioned above, the gas temperature in the GAP is fairly high (around 3000 K), and the VDFs of both CO_2 and N_2 are thermal (see Figure S14), and thermal reactions are important for the CO_2 and N_2 conversion at this high temperature. Nevertheless, the CO_2 and N_2 molecules are first activated by electron impact excitation. To show the contribution of plasma in the CO_2 and N_2 conversion, we plot in Figure 7 the calculated absolute CO_2 and N_2 conversion in the GAP as a function of N_2 fraction in the mixture, comparing with plasma and without plasma (i.e., only thermal reactions, without electron impact reactions). It is clear that, because of the high temperature, thermal reactions are indeed most important. Indeed, although the VDF is thermal, the higher vibrational levels are still sufficiently populated at this high temperature, to cause dissociation. Nevertheless, the conversion in case of plasma is still somewhat higher than the pure thermal conversion, especially at higher N_2 fractions, because the electron impact reactions create extra reactive species for the thermal reactions.

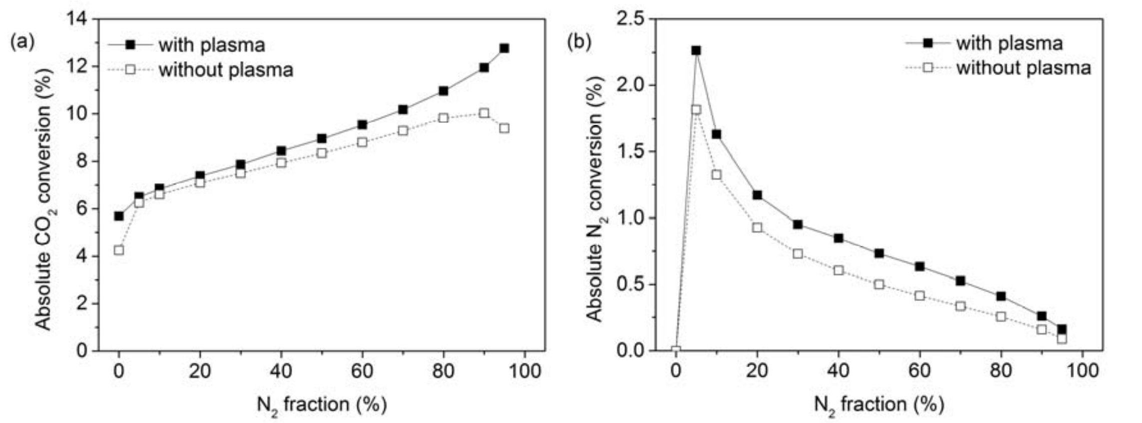

Figure 7. Calculated absolute CO_2 (a) and N_2 (b) conversion in the GAP as a function of N_2 fraction in the mixture, comparing with plasma and without plasma (i.e., only thermal reactions, without electron impact reactions)

Comparison of GAP with DBD

As mentioned in the Introduction, Snoeckx et al.[28] have also analyzed the byproducts formed in a CO_2/N_2 mixture, but for a DBD plasma, which has completely different plasma properties than a GAP,[2] hence affecting the plasma chemistry. Therefore, we compare here both plasma reactors in terms of conversion efficiency and byproduct formation, at typical GAP and DBD conditions, i.e., a specific energy input (SEI) of around 2 kJ/L and 12 kJ/L, respectively. These values originate from a plasma power of 350 W and a total flow rate of 10 L/min for the GAP, while the plasma power and total flow rate in the DBD reactor are around 120 W and 611 mL/min, respectively. Note that we cannot compare the results in the GAP and DBD at the same SEI, because the flow rate in the GAP is much higher, which is necessary to obtain a good vortex flow pattern, while such a high flow rate would result in very small residence times, and thus virtually no conversion, in a DBD. However, this difference in flow rate (and power) must be accounted for when we compare the results in the GAP and DBD.

CO_2 conversion, energy cost and energy efficiency

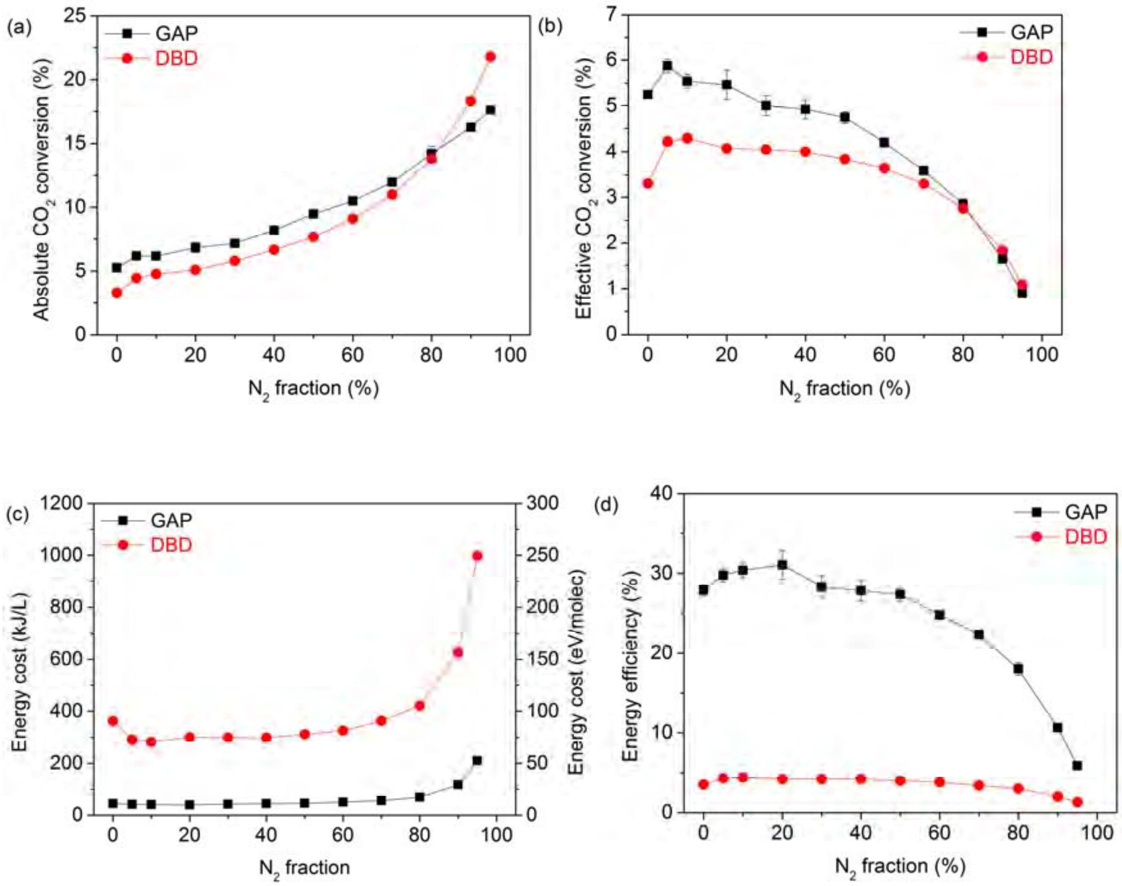

Figure 8. Absolute (a) and effective (b) CO_2 conversion, energy cost (c) and energy efficiency (d), as a function of N_2 fraction, both for the GAP and DBD. The error bars are included in the graphs, but are sometimes too small to be visible.

In Figure 8(a), the absolute CO_2 conversion is plotted for both plasma reactors as a function of N_2 fraction. The GAP shows a slightly more than linear trend with increasing N_2 fraction, while the trend of the DBD is more exponential. The absolute values in the GAP are somewhat higher than in the DBD, even at much lower SEI (cf. above). Only at the highest N_2 fractions, the values are higher in the DBD (i.e., 22 % vs 18 %). Thus, in general the CO_2 conversion is higher in the GAP, but the addition of large amounts of N_2 in a DBD enhances the CO_2 conversion more compared to in a GAP. To explain this, we should compare the main dissociation mechanisms of CO_2 in DBD and GAP. In a DBD the main dissociation mechanism is electron impact dissociation of ground state CO_2, but with increasing N_2 fraction, the reaction of CO_2 with metastable N_2 molecules becomes more important, and is the most important dissociation mechanism above 70% N_2 addition.[28] In our GAP, the reaction of vibrationally excited CO_2 with dissociated N_2 products, i.e., mainly NO but also CN (Figure S8(a)), is the most important CO_2 dissociation process. The reaction with NO is dominant up to 80% N_2, while above 80 %, the reaction with CN becomes most important, but its absolute rate is quite low (Figure S8(a)), because CN also needs C to be formed, which is low at low CO_2 fractions. Thus, at high N_2 fractions, the contribution of N_2 is more important in a DBD than in a GAP, explaining why the GAP and DBD curves intersect at ca. 80% N_2. As is clear from Figure 8(b), the effective CO_2 conversion is higher in the GAP than in the DBD, except again at N_2 fractions above 80 %, where the values are comparable. The energy cost in the DBD is on average 6 times higher than in the GAP; see Figure 8(c). Indeed, the effective conversion is slightly lower, but the SEI in the plasma is much higher (12 kJ/L vs 2 kJ/L). Thus, our GAP is much more promising than a DBD for plasma-based CO_2 conversion[2]. The energy efficiency in both plasma reactors decreases with increasing N_2 fraction (see Figure 8(d)). In addition, the energy efficiency is 7 times higher in the GAP than in the DBD, for N_2 fractions up to 50 %, i.e., around 27 – 31 % for the GAP vs. 4% for the DBD. At N_2 fractions above 50 %, the difference becomes smaller, as the values drop to 5.9 % for the GAP and 1.3 % for the DBD, at 95 % N_2. Indeed, in the DBD, the main mechanism of CO_2 dissociation is electron impact dissociation from ground state CO_2 molecules[28], which requires much more energy than the vibrational pathway in the GAP, this explains the better energy efficiency in the GAP than in the DBD.

Byproduct formation

We can conclude from above that the GAP is definitely superior for CO_2 conversion in the presence of N_2, in terms of conversion efficiency. However, for industrial application, also the formation of byproducts is important. The concentrations of NO and NO_2, obtained in the GAP and DBD are compared in Figure 9, as a function of N_2 fraction in the mixture.

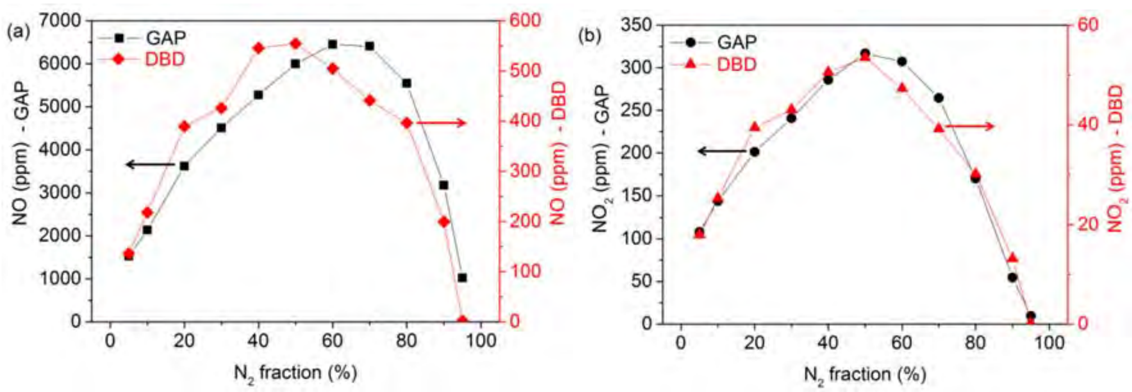

Figure 9. NO (a) and NO_2 (b) concentration as a function of N_2 fraction, both for the GAP and DBD. The error bars are included in the graphs, but are too small to be visible.

Both the NO and NO_2 concentrations follow the same trend as a function of N_2 fraction in the GAP and DBD, with a maximum around 50-60% N_2. This is striking, as the formation mechanisms in both plasma types are quite different (see ref. [28]). However, the reason is that in both mechanisms important in GAP and DBD, both N_2 and CO_2 first have to be split into reactive species needed for NO formation, and this condition is fulfilled most when both N_2 and CO_2 are present in somewhat equal amounts. Indeed, in both GAP and DBD, when there is mainly N_2 in the mixture, CO_2 will be the limiting reactant for NO formation, while in case of mainly CO_2 in the mixture, N_2 will be the limiting reactant.

However, the NO and NO_2 concentrations are more than 10 times and about 6 times higher in the GAP than in the DBD. This can only partly be explained by the higher effective CO_2 conversion (Figure 8(b)). Indeed, the N_2 dissociation – also needed for NOx formation – is a factor 4 higher in the GAP than in the DBD (i.e., 4 % vs. 1%). In addition, the selectivity towards NO and NO_2 is significantly higher in the GAP than in the DBD, where also other NOx compounds were formed[28].

It is indeed remarkable that in our GAP no N_2O, N_2O_3 and N_2O_5 could be detected, while they were clearly detected in the DBD, with the same measuring equipment (FTIR)[28]. Our simulation results also

indicate NO and NO_2 as the major byproducts of CO_2 and N_2 conversion in the GAP, in agreement with our experiments, while N_2O (0.1 – 3 ppm), N_2O_3 (10^{-8} – 10^{-7} ppm), N_2O_4 (10^{-11} – 10^{-9} ppm) and N_2O_5 (10^{-12} – 10^{-10} ppm) have much lower concentrations (Figure S16(a)). In comparison, in a DBD, next to NO and NO_2 also N_2O and N_2O_5 are formed in relatively high concentrations, i.e., calculated up to 115 ppm for NO, 34 ppm for NO_2, 55 ppm for N_2O, and even up to 1000 ppm for N_2O_5; see Figure S16(b) and also ref. 28. The N_2O_3 and N_2O_4 concentrations are calculated to be much lower.
The reason we only detected NO and NO_2 in our experiments, while in the DBD also N_2O, N_2O_3 and N_2O_5 were detected, is attributed to the different plasma temperature. It is predicted to be around 3000 K inside the arc[51] in our GAP (for pure CO_2), which is too high to form N_2O, N_2O_3 and N_2O_5. Indeed, at higher temperatures the formation rates of these species increase but the loss rates are even higher (Figure S17), which results in lower net concentrations (Figure S16). On the other hand, a DBD operates around room temperature, yielding higher formation than loss rates (Figure S17), resulting in higher net concentrations (Figure S16). Furthermore, DBD plasmas are characterized by streamers, with short lifetime (order of 30 ns[61]), in which mainly electron impact reactions occur, but in between these streamers, NO_2 can interact with NO or NO_3 to form N_2O_3 and N_2O_5 respectively[28]. This is not the case in a GAP, because the arc is continuously stabilized in the center, explaining why only NO and NO_2 are detected in our experiments.

Taking into account that N_2O is a very potent greenhouse gas, with a global warming potential (GWP) of 298 $CO_{2,\mathrm{equivalent}}$, it is highly beneficial that its concentration in the GAP does not exceed the detection limit of 1 ppm. After all, the production of N_2O would void the greenhouse gas mitigation potential of plasma technology if no denox purification step would be added.

Overall we can conclude that the GAP is far superior for CO_2 conversion in the presence of N_2 than the DBD, due to the higher conversion, but especially the absence of N_2O, N_2O_3, N_2O_5 formation, and the significantly higher energy efficiency.

Conclusions

We have investigated the effect of N_2 on CO_2 conversion in a GAP, by combining experiments and simulations. The addition of N_2 has a positive effect on the absolute CO_2 conversion up to 50 %, while at higher N_2 fractions, the effective CO_2 conversion and energy efficiency drop. Our simulations reveal that the CO_2 conversion mainly proceeds through the vibrational levels, which are populated through collision with the N_2 vibrational levels. In addition, NO and NO_2 are formed in the CO_2/N_2 mixture, initiated by the reaction between N_2 vibrational levels and O atoms (so-called Zeldovich mechanism[24]).

Combining CO_2 and N_2 in a GAP thus can lead to combined CO_2 conversion and N_2 fixation. The highest amount of NOx obtained is 6761 ppm, which is still below the minimum threshold of 1 % to make it effective for N_2 fixation. By improving our reactor and gas inlet design, we should be able to enhance the gas fraction that passes through the arc, and thus the CO_2 conversion and NOx production. This optimization will need dedicated fluid dynamics simulations, which are planned in our future work.

We compared the performance of our GAP with other plasma types. The best energy efficiency for CO_2 conversion is reached in our GAP, but the conversion itself needs further improvement. In terms of NOx production, the NOx yield is still quite low (attributed to the limited CO_2 conversion), but the energy consumption is reasonable compared to other plasma types, certainly if we take into account that our energy consumption also includes the cost for CO_2 conversion.

Finally, we made a more detailed comparison with a DBD, which is the only other work in literature where NOx production was also studied from a CO_2/N_2 mixture. The energy efficiency was 7 times higher in our GAP than in the DBD, next to a somewhat higher CO_2 conversion. Indeed, CO_2 dissociation in the GAP proceeds through vibrationally excited states, while in a DBD it occurs mainly by electronic excitation, which is less efficient[2]. Furthermore, our GAP only produces NO and NO_2, while N_2O, N_2O_3 and N_2O_5 are also formed in a DBD. Keeping in mind that N_2O is a very potent greenhouse gas, it is highly beneficial that its concentration in the GAP does not exceed the detection limit of 1 ppm. Overall, the GAP is superior for CO_2 conversion in the presence of N_2 compared to a DBD, due to its higher conversion, but especially the absence of N_2O, N_2O_3, N_2O_5 formation and the much higher energy efficiency.

Acknowledgements

We acknowledge financial support from the Fund for Scientific Research Flanders (FWO; Grant no. G.0383.16N) and the Excellence of Science program of the Fund for Scientific Research (FWO-FNRS; Grant no. G0F9618N; EOS ID: 30505023). The calculations were performed using the Turing HPC infrastructure at the CalcUA core facility of the Universiteit Antwerpen (UAntwerpen), a division of the Flemish Supercomputer Center VSC, funded by the Hercules Foundation, the Flemish Government (department EWI) and the UAntwerpen. Finally, we also want to thank Dr. Ramses Snoeckx for the very interesting discussions, and A. Fridman and A. Rabinovich for developing the GAP.

References

1 I. Adamovich, S. D. Baalrud and A. Bogaerts, *J. Phys. D. Appl. Phys.*, 2017, **50**, 323001.

2 R. Snoeckx and A. Bogaerts, *Chem. Soc. Rev.*, 2017, **46**, 5805–5863.

3 A. Bogaerts, E. Neyts, R. Gijbels and J. van der Mullen, *Spectrochim. Acta, Part B*, 2002, **57**, 609–658.

4 T. Nunnally, K. Gutsol, A. Rabinovich, A. Fridman, A. Gutsol and A. Kemoun, *J. Phys. D. Appl. Phys.*, 2011, **44**, 274009.

5 M. Ramakers, G. Trenchev, S. Heijkers, W. Wang and A. Bogaerts, *ChemSusChem*, 2017, **10**, 2642–2652.

6 O. Mutaf-Yardimci, A. V. Saveliev, A. a. Fridman and L. a. Kennedy, *J. Appl. Phys.*, 2000, **87**, 1632.

7 A. Czernichowski, H. Nassar, A. Ranaivosoloarimanana, A. A. Fridman, M. Simek, K. Musiol, E. Pawelec and L. Dittrichova, *Acta Phys. Pol. A*, 1996, **89**, 595–603.

8 J. Zhu, A. Ehn, J. Gao, C. Kong, M. Aldén, M. Salewski, F. Leipold, Y. Kusano and Z. Li, *Opt. Express*, 2017, **25**, 20243.

9 F. Richard, J. M. Cormier, S. Pellerin and J. Chapelle, *J. Appl. Phys.*, 1996, **79**, 2245.

10 J. Zhu, J. Gao, A. Ehn, M. Aldén, Z. Li, D. Moseev, Y. Kusano, M. Salewski, A. Alpers, P.

Gritzmann and M. Schwenk, *Appl. Phys. Lett.*, 2015, **106**, 044101.

11 E. Cleiren, S. Heijkers, M. Ramakers and A. Bogaerts, *ChemSusChem*, 2017, **10**, 4025–4036.

12 J. L. Liu, H. W. Park, W. J. Chung and D. W. Park, *Plasma Chem. Plasma Process.*, 2015, **36**, 437–449.

13 F. Zhu, H. Zhang, X. Yan, J. Yan, M. Ni, X. Li and X. Tu, *Fuel*, 2017, **199**, 430–437.

14 A. Wu, J. Yan, H. Zhang, M. Zhang, C. Du and X. Li, *Int. J. Hydrogen Energy*, 2014, **39**, 17656–17670.

15 X. Tu and J. C. Whitehead, *Int. J. Hydrogen Energy*, 2014, **39**, 9658–9669.

16 A. Indarto, D. R. Yang, J. W. Choi, H. Lee and H. K. Song, *J. Hazard. Mater.*, 2007, **146**, 309–315.

17 J. L. Liu, H. W. Park, W. J. Chung, W. S. Ahn and D. W. Park, *Chem. Eng. J.*, 2016, **285**, 243–251.

18 K. Li, J. L. Liu, X. S. Li, X. Zhu and A. M. Zhu, *Chem. Eng. J.*, 2016, **288**, 671–679.

19 C. S. Kalra, Y. I. Cho, A. Gutsol, A. Fridman and T. S. Rufael, *Rev. Sci. Instrum.*, 2005, **76**, 1–7.

20 L. Bromberg, D. R. Cohn, A. Rabinovich, J. E. Surma and J. Virden, *Int. J. Hydrogen Energy*, 1999, **24**, 341–350.

21 A. Jess, P. Kaiser, C. Kern, R. Unde and C. Von Olshausen, *Chemie-Ingenieur-Technik*, 2011, **83**, 1777–1791.

22 M. Aresta, A. Dibenedetto and A. Angelini, *Chem. Rev.*, 2014, **114**, 1709–1742.

23 B. S. Patil, Q. Wang, V. Hessel and J. Lang, *Catal. Today*, 2015, **256**, 49–66.

24 W. Wang, B. Patil, S. Heijkers, V. Hessel and A. Bogaerts, *ChemSusChem*, 2017, **10**, 2145–2157.

25 A. Bogaerts and E. C. Neyts, *ACS Energy Lett.*, 2018, **3**, 1013–1027.

26 S. Heijkers, R. Snoeckx, T. Kozák, T. Silva, T. Godfroid, N. Britun, R. Snyders and A. Bogaerts, *J. Phys. Chem. C*, 2015, **119**, 12815–12828.

27 T. Silva, N. Britun, T. Godfroid and R. Snyders, *Plasma Sources Sci. Technol.*, 2014, **23**, 025009.

28 R. Snoeckx, S. Heijkers, K. Van Wesenbeeck, S. Lenaerts and A. Bogaerts, *Energy Environ. Sci.*, 2016, **9**, 30–39.

29 S. Heijkers and A. Bogaerts, *J. Phys. Chem. C*, 2017, **121**, 22644–22655.

30 L. F. Spencer and A. D. Gallimore, *Plasma Sources Sci. Technol.*, 2013, **22**, 015019.

31 A. Fridman, *Plasma Chemistry*, Cambridge University Press, New York, 2008.

32 B. S. Patil, 2017.

33 B. S. Patil, F. J. J. Peeters, J. A. Medrano, F. Gallucci, W. Wang, A. Bogaerts, Q. Wang, G. Van Rooij, J. Lang and V. Hessel, *Appl. Energy*, 2018, Submitted.

34 Z. Bo, J. Yan, X. Li, Y. Chi and K. Cen, *J. Hazard. Mater.*, 2009, **166**, 1210–1216.

35 A. Evans, R. Luebke and C. Petit, *J. Mater. Chem. A*, 2018, **6**, 10570–10594.

36 T. Namihira, S. Katsuki, R. Hackam, H. Akiyama and K. Okamoto, *IEEE Trans. Plasma Sci.*, 2002, **30**, 1993−1998.

37 J. F. Coudert, J. M. Baronnet, J. Rakowitz and P. Fauchais, in *Synthesis of nitrogen oxides in a plasma produced by a jet arc generator*, 1977.

38 M. Rahman and V. Cooray, *Opt. Laser Technol.*, 2003, **35**, 543−546.

39 W. Bian, X. Song, J. Shi and X. Yin, *J. Electrost.*, 2012, **70**, 317−326.

40 N. Rehbein and V. Cooray, *J. Electrost.*, 2001, **51−52**, 333−339.

41 V. M. Shmelev, A. V. Saveliev and L. A. Kennedy, *Plasma Chem. Plasma Process.*, 2009, **29**, 275−290.

42 B. S. Patil, N. Cherkasov, J. Lang, A. O. Ibhadon, V. Hessel and Q. Wang, *Appl. Catal., B*, 2016, **194**, 123−133.

43 B. Mutel, O. Dessaux and P. Goudmand, *Rev. Phys. Appl.*, 1984, **19**, 461−464.

44 L. S. Polak, A. A. Ovsiannikov, D. I. Slovetsky and F. B. Vurzel, *Theoretical and Applied Plasma Chemistry*, Nauka (Science), Moscow, 1975.

45 R. I. Asisov, V. K. Givotov, V. D. Rusanov and A. Fridman, *Sov. Phys. High Energy Chem. (Khimia Vysok. Energ.*, 1980, **14**, 366.

46 T. Kim, S. Song, J. Kim and R. Iwasaki, *Jpn. J. Appl. Phys.*, 2010, **49**, 126201.

47 M. A. Malik, C. Jiang, R. Heller, J. Lane, D. Hughes and K. H. Schoenbach, *Chem. Eng. J.*, 2016, **283**, 631−638.

48 K. Birkeland, *Trans. Faraday Soc.*, 1906, **2**, 98−116.

49 J. Krop and I. Pollo, *Chemia*, 1981, **678**, 51−59.

50 R. Ingels, D. Graves, S. Anderson and R. Koller, *Int. Fertil. Soc. Conf.*, 2015, 1–27.

51 G. Trenchev, S. Kolev, W. Wang, M. Ramakers and A. Bogaerts, *J. Phys. Chem. C*, 2017, **121**, 24470–24479.

52 J. G. Chen, R. M. Crooks, L. C. Seefeldt, K. L. Bren, R. Morris Bullock, M. Y. Darensbourg, P. L. Holland, B. Hoffman, M. J. Janik, A. K. Jones, M. G. Kanatzidis, P. King, K. M. Lancaster, S. V. Lymar, P. Pfromm, W. F. Schneider and R. R. Schrock, *Science (80-.).*, 2018, **360**.

53 L. Wang, M. Xia, H. Wang, K. Huang, C. Qian, C. T. Maravelias and G. A. Ozin, *Joule*, 2018, **2**, 1055–1074.

54 R. Lan, K. A. Alkhazmi, I. A. Amar and S. Tao, *Appl. Catal. B Environ.*, 2015, **152**–**153**, 212–217.

55 P. Peng, P. Chen, C. Schiappacasse, N. Zhou, E. Anderson, D. Chen, J. Liu, Y. Cheng, R. Hatzenbeller, M. Addy, Y. Zhang, Y. Liu and R. Ruan, *J. Clean. Prod.*, 2018, **177**, 597–609.

56 A. J. Martín, T. Shinagawa and J. Pérez-Ramírez, *Chem*, 2018, https://doi.org/10.1016/j.chempr.2018.10.010.

57 N. Cherkasov, A. O. Ibhadon and P. Fitzpatrick, *Chem. Eng. Process. Process Intensif.*, 2015, **90**, 24–33.

58 T. Kozák and A. Bogaerts, *Plasma Sources Sci. Technol.*, 2014, **23**, 045004.

59 A. Bogaerts, T. Kozák, K. van Laer and R. Snoeckx, *Faraday Discuss.*, 2015, **183**, 217–232.

60 A. Berthelot and A. Bogaerts, *Plasma Sources Sci. Technol.*, 2016, **25**, 045022.

61 A. Ozkan, T. Dufour, T. Silva, N. Britun, R. Snyders, A. Bogaerts and F. Reniers, *Plasma Sources Sci. Technol.*, 2016, **25**.

Supplementary information

Combining CO_2 conversion and N_2 fixation in a gliding arc plasmatron

Marleen Ramakers[a], Stijn Heijkers[a], Tom Tytgat[b], Silvia Lenaerts[b] and Annemie Bogaerts[a]

[a] Research group PLASMANT, Department of Chemistry, University of Antwerp, Universiteitsplein 1, 2610 Antwerp, Belgium
[b] Research group DuEL, Department of Bioscience engineering, University of Antwerp, Groenenborgerlaan 171, 2020 Antwerp, Belgium

Description of the experiments

Product analysis

The feed gases and main product gases (CO_2, N_2, CO, O_2) were analyzed by a three-channel compact gas chromatograph (CGC) from Interscience. This device has three different ovens, each with their own column and detector. A Molsieve 5A and Rt-Q-Bond column were used to separate O_2, N_2 and CO, which were detected with a thermal conductivity detector (TCD). The other channel was equipped with a Rt-Q-Bond column and TCD for the measurement of CO_2. The absolute conversion of CO_2, X_{abs,CO_2}, is defined as:

$$X_{abs,CO_2}(\%) = \frac{\dot{n}_{CO_{2(in)}} - \dot{n}_{CO_{2(out)}}}{\dot{n}_{CO_{2(in)}}} \times 100\% \qquad (1)$$

where $\dot{n}_{CO_{2(in)}}$ and $\dot{n}_{CO_{2(out)}}$ are the molar flow rate of CO_2 without and with plasma, respectively. As the method mentioned above does not account for the gas expansion due to CO_2 splitting, a correction factor is used, which is explained in ref. 1.

The effective conversion, X_{eff,CO_2}, accounts for the fraction of CO_2 in the initial gas mixture:

$$X_{eff,CO_2}(\%) = X_{abs,CO_2}(\%) \times fraction_{CO_2} \qquad (2)$$

To calculate the energy cost and energy efficiency of CO_2 conversion, the specific energy input (SEI) in the plasma is defined as:

$$SEI\left(\frac{kJ}{L}\right) = \frac{Plasma\ power\ (kW)}{Flow\ rate\ (\frac{L_n}{min})} \times 60\left(\frac{s}{min}\right) \qquad (3)$$

where the flow rate is expressed in L_n/min (liters normal per minute) with reference conditions at a temperature of 0 °C and a pressure of 1 atm.
The energy cost (EC) for converting CO_2 is calculated as follows:

$$EC_{CO_2}\left(\frac{kJ}{L}\right) = \frac{SEI\left(\frac{kJ}{L}\right)}{X_{eff,CO_2}} \qquad (4)$$

Likewise, the energy efficiency, η, is calculated as:

$$\eta(\%) = \frac{\Delta H_R\left(\frac{kJ}{mol}\right) \times X_{eff,CO_2}(\%)}{SEI\left(\frac{kJ}{L}\right) \times 22.4\left(\frac{L}{mol}\right)} \qquad (5)$$

where ΔH_R is the reaction enthalpy of CO_2 splitting (i.e., 279.8 kJ/mol), and 22.4 L/mol is the molar volume at 0 °C and 1 atm.

During the experiments, the concentrations of NO, NO_2, and other NOx compounds were monitored almost in real-time using a Nicolet 380 Fourier Transform Infrared (FTIR) Spectrometer (Thermo Fischer Scientific, Waltham, MA) equipped with a 2m heated gas cell with ZnSe windows and a DTGS detector. Based on the height of the bands, different species were monitored at the following wavenumbers: NO with ν(NO) at 1900 cm^{-1} and NO_2 with $\nu_{as}(NO_2)$ at 1597 cm^{-1}. Note that N_2O with ν(NN) at 2234 cm^{-1}, N_2O_3 with $\nu_s(NO_2)$ at 1309 cm^{-1}, N_2O_5 with $\nu_s(NO_2)$ at 1245 cm^{-1}, O_3 with ν_s at 1054 cm^{-1} were never detected with the FTIR spectrometer. To quantify these results, the concentrations were determined using a CT5800 Analyzer (Emerson, Stirling, UK) based on Quantum Cascade Laser Technology, allowing to accurately measure different N-containing molecules simultaneously. The monitored compounds were NO, NO_2, N_2O and NH_3, with the following detection limits: 1.5 ppm, 0.5 ppm, 1 ppm and 1 ppm, respectively.

Description of the model

Details of the 0D model

The 0D model is based on solving equation (6):

$$\frac{\partial n_s}{\partial t} = \sum_{i=1}^{j}[(a_{s,i}^R - a_{s,i}^L)R_i] \tag{6}$$

where n_s is the density of species s (in m^{-3}) , j the total number of reactions, $a_{s,i}^L$ and $a_{s,i}^R$ the stoichiometric coefficients at the left hand side and right hand side of the reaction and R_i the rate of reaction (in m^{-3} s^{-1}), given by:

$$R_i = k_i \prod_s n_s^{\alpha_{s,i}} \tag{7}$$

where k_i is the rate coefficient (in m^3 s^{-1} or m^6 s^{-1} for two-body or three-body reactions, respectively). The rate coefficients of the heavy particle reactions are either constant or dependent on the gas temperature, whereas the rate coefficients of the electron impact reactions depend on the electron temperature T_e or the reduced electric field E/N (i.e., the electric field E divided by the number density of all neutral species N, usually expressed in Td = 10^{-21} V m^2). The rate coefficients of the electron impact reactions are generally calculated according to the following equation:

$$k_i = \int_{\varepsilon_{th}}^{\infty} \sigma_i(\varepsilon) v(\varepsilon) f(\varepsilon) d\varepsilon \tag{8}$$

with ε the electron energy (usually in eV), ε_{th} the minimum threshold energy needed to induce the reaction, $v(\varepsilon)$ the velocity of the electrons (in m s^{-1}) , $\sigma_i(\varepsilon)$ the cross section of collision i (in m^2), and $f(\varepsilon)$ the normalized electron energy distribution function (EEDF; in eV^{-1}) calculated using a Boltzmann solver. In this work we use the ZDPlasKin[2] code to solve the balance equations (equation (6)) of all species, which has a built-in Boltzmann solver, called BOLSIG+ [3], to calculate the EEDF and the rate coefficients of the electron impact reactions based on a set of cross sections, the plasma composition, the gas temperature and the reduced electric field (E/N). The electric field (E; in V m^{-1}) is calculated from a given power density, using the so-called local field approximation [4]:

$$E = \sqrt{\frac{P}{\sigma}} \tag{9}$$

with P the input power density (in W m^{-3}) and σ the plasma conductivity (A V^{-1} m^{-1}). The plasma conductivity is estimated at the beginning of the simulations as [4]:

$$\sigma = \frac{e^2 n_{e,init}}{m_e v_m} \tag{10}$$

with e the elementary charge (1.6022x10^{-19} C), $n_{e,init}$ the initial electron density (in m^{-3}), m_e the electron mass (9.1094x10^{-31} kg) and v_m the collision frequency (in s^{-1}) calculated using BOLSIG+ [3]. During the simulation the plasma conductivity is calculated as [4]:

$$\sigma = \frac{e v_d n_e}{(\frac{E}{N})_{prev} n_0} \tag{11}$$

with v_d the electron drift velocity (in m s^{-1}), which is calculated using BOLSIG+ [3] implemented in ZDPlasKin, and $(\frac{E}{N})_{prev}$ the reduced electric field at the previous time step (in V m^2).

The balance equation for the gas temperature T_g (in K) is also solved, but for pure CO_2. We only do this to estimate when the maximum gas temperature is reached (i.e. 3140 K), which is derived from 3D fluid dynamics simulations[5] and experiments [6]. The same approach was also used in 7,8. We assume that the temperature profile will not significantly change when adding N_2 to the mixture [6].
The balance equation for the gas temperature is:

$$N \frac{\gamma k}{\gamma - 1} \frac{dT_g}{dt} = P_{e,el} + \sum_j R_j \Delta H_j - P_{ext} \tag{12}$$

where $N = \sum n_i$ is the total neutral species density, γ is the specific heat ratio of the total gas mixture, k is the Boltzmann constant (in J K^{-1}), $P_{e,el}$ is the gas heating power density due to elastic electron-neutral collisions (in W m^{-3}), R_j is the rate of reaction j (in m^{-3} s^{-1}), ΔH_j is the heat released (or consumed when this value is negative) by reaction j (in J) and P_{ext} is the heat loss due to energy exchange with the surroundings (in W m^{-3}). The specific heat ratio of the total (ideal) gas mixture is calculated from the specific heat ratios of the individual species in the model, γ_i, using the formula:

$$N \frac{\gamma}{\gamma - 1} = \sum_i n_i \frac{\gamma_i}{\gamma_i - 1} \tag{13}$$

where n_i are the densities of the individual species i. The individual specific heat ratios, γ_i, can be calculated from the specific heat capacity at constant pressure $c_{p,i}$ (in J K^{-1} kg^{-1}) using the relation:

$$c_{p,i} = \frac{\gamma_i}{\gamma_i - 1} \frac{k}{M} \tag{14}$$

where k is the Boltzmann constant and M is the molar weight of CO_2 (in kg). Since the vibrational levels are treated as separate species (see Table S1), only the heat capacity due to translational and rotational degrees of freedom and, in the case of CO_2, also the heat capacity due to the symmetric vibrational modes, which are not treated as individual species, should be taken into account [9,10]. A classical partitioning between the translational and rotational degrees of freedom is assumed, which gives a value for the specific heat ratio, at room temperature and above, of 1.67 for the atomic species and 1.40 for the diatomic molecules (CO, O_2 and C_2). For O_3, a value of 1.27 was taken [9,11]. Details about the calculation of the total heat capacity and the resulting specific heat ratio for CO_2, calculated using equation (14), can be found in 9.

Modeling the GAP with a 0D approach

The model is applied to the GAP reactor used for the experiments, using exactly the same dimensions and operating conditions as in the experiments. A schematic diagram of the GAP, including the dimensions, is presented in Figure S1. The arc plasma column inside the GAP is illustrated by the red rectangle. Because the gas enters the GAP reactor by tangential inlets, it follows a vortex flow pattern. As the outlet (anode) diameter is smaller than the reactor body (cathode part) (see Figure S1), the gas will first move upwards in a so-called forward vortex flow (indicated in Figure S1 by the solid spiral) and when it arrives at the top of the reactor, it will have lost some speed by friction and inertia, so that it will travel downwards in a smaller so-called reverse vortex flow, which is more or less captured by the arc column (see dashed spiral in figure S1). This vortex flow results in stabilization of the arc column in the center of the GAP reactor, as predicted by 3D fluid dynamics modeling [5,12]. Since the plasma confined in the inner vortex gas flow is more or less uniform, [5,12] we can assume a constant power density applied to the gas, during its residence time in the plasma column. Hence, 0D modeling of this kind of plasma is justified. Indeed, the 0D model calculates the species densities as a function of time, and spatial variation by means of transport is not considered. Nevertheless, by means of the gas flow rate, we can convert the temporal variation calculated in the model into a spatial variation in the arc plasma column, and vice versa. The arc plasma column is thus considered as a plug flow reactor, where the plasma characteristics vary as a function of distance travelled by the gas within a certain residence time, in the same way as they would vary as a function of time in a batch reactor. 2D fluid dynamics simulation results of Trenchev et al. for a GAP in argon [5,12] revealed that the arc radius is typically around 1 mm. However, the temperature just outside this arc region is still high enough to induce plasma, especially in a molecular plasma where vibration-translation (VT) relaxation causes gas heating. Therefore, we assumed an arc radius of 2 mm in our simulations. Combined with the length of the cathode (10.20 mm) and anode (16.30 mm) and the inlet of 3 mm (see Figure S1), this yields a plasma volume of 0.37 cm^3. These approaches were also successfully used in 1,7,8.
The CO_2 conversion after passing through the arc, $X_{CO_2,arc}$, is defined as:

$$X_{CO_2,arc}(\%) = 100\% \left(1 - \frac{n_{CO_2,e}\, v_e}{n_{CO_2,i}\, v_i}\right) \quad (15)$$

where $n_{CO_2,e}$ and v_e are the CO_2 density (in m^{-3}) and gas velocity (in m s^{-1}) at the end of the arc region near the outlet (fixed at 3140 K), and $n_{CO_2,i}$ and v_i are the CO_2 density (in m^{-3}) and gas velocity (in m s^{-1}) at the beginning, right before entering the arc region, i.e., at room temperature.

Since not all gas in the reactor passes through the arc region, the total CO_2 conversion in the reactor, which is also measured experimentally, will be lower than the CO_2 conversion after passing through the arc region, as we also need to account for the unconverted CO_2 in the reactor. This total conversion, $X_{CO_2,tot}$, is defined as:

$$X_{CO_2,tot}(\%) = 100\% (1 - \frac{Q_{CO_2,arc} + Q_{CO_2,,rest}}{Q_{CO_2,in}}) \quad (16)$$

where $Q_{CO_2,in}$, $Q_{CO_2,arc}$ and $Q_{CO_2,,rest}$ are the CO_2 fluxes (in s^{-1}) entering the reactor, exiting the arc region at the outlet and exiting the reactor without passing through the arc, hence without being converted. This means that we need to define the fraction of CO_2 that passes through the arc region, which is explained below.

The CO_2 flux entering the reactor $Q_{CO_2,in}$ is defined as:

$$Q_{CO_2,in} = n_{CO_2,i}\, \dot{V} \tag{17}$$

where $n_{CO_2,i}$ is the CO_2 density (in m^{-3}) at the inlet of the reactor (at room temperature) and $\dot{V}$ the volumetric flow rate (in m^3 s^{-1}). The CO_2 flux exiting the arc region at the outlet $Q_{CO_2,arc}$ is defined as:

$$Q_{CO_2,arc} = n_{CO_2,e}\, v_e\, A_{arc} \tag{18}$$

with $n_{CO_2,e}$ and v_e the CO_2 density (in m^{-3}) and gas velocity (in m s^{-1}) at the end of the arc region near the outlet, and A_{arc} the cross sectional area of the arc region, i.e. 12.57 mm^2 . Finally, due to conservation of mass, the CO_2 flux $Q_{CO_2,,rest}$ which is not treated by the plasma, is given by:

$$Q_{CO_2,rest} = Q_{CO_2,in} - n_{CO_2,i}\, v_i\, A_{arc} \tag{19}$$

Hence, the fraction of CO_2 that passes through the arc region is defined by the mass flow rate through the arc, and is 14.8 % of the total mass flow rate through the reactor. The remaining 85.2% does not pass through the arc, and will not be converted.

The N_2 conversion is calculated in exactly the same way as the CO_2 conversion.

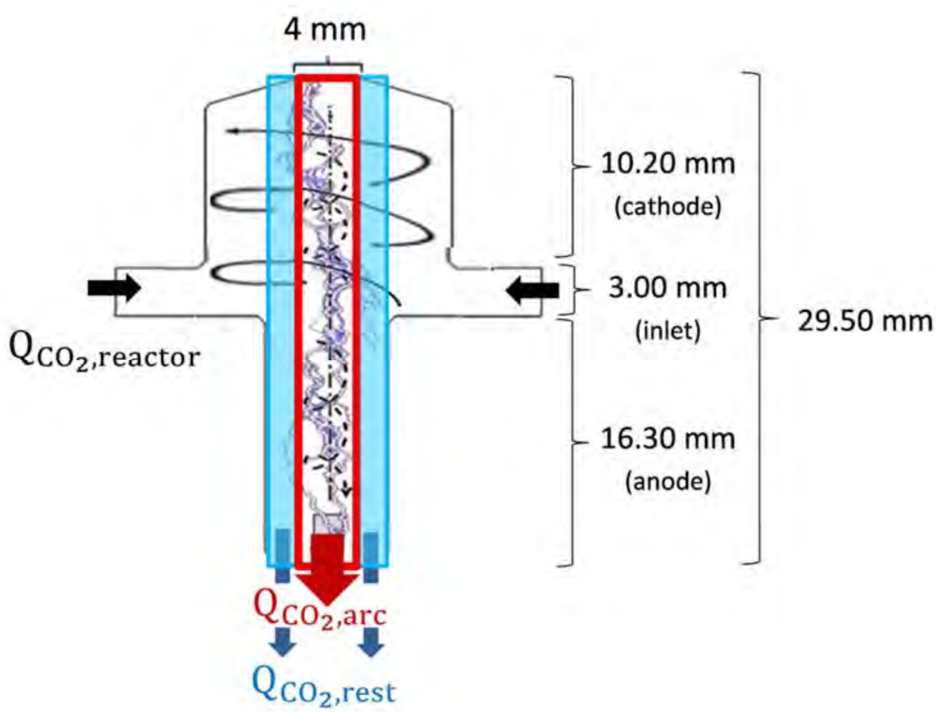

Figure S1. Schematic picture of the GAP, with indication of the dimensions, as well as the outer vortex (solid spiral) and inner (reverse) vortex (dashed spiral). The red frame indicates the arc plasma column, while the blue part indicates the region where the gas is untreated in the reverse vortex.

Chemistry set

The chemistry set used in this study is based on the papers of Heijkers et al. [13], Snoeckx et al. [14] and Wang et al.[15]. The species included in the model are listed in Table S1. The symbol 'V' between brackets for N_2, CO_2, CO and O_2 and the symbol 'E' between brackets for CO_2, CO and O_2 represent the vibrationally and electronically excited levels of these species, respectively. More information about the notation of the vibrationally and electronically excited levels of CO_2, CO and O_2 can be found in [16].

For CO_2, all 21 levels of the asymmetric mode till the dissociation limit (5.5 eV) are taken into account, since they are crucial for storing vibrational energy for efficient CO_2 dissociation [17]. In addition, four effective low-lying symmetric stretching and bending mode levels are included in the model, i.e. CO_2 (Va-Vd). For N_2, up to 24 vibrational levels are included (till 5.8 eV), which is more than enough to describe vibration induced dissociation in the GAP, since most dissociation occurs from the lowest levels (see Figure S2), which is also the case for pure CO_2, as revealed in 8.

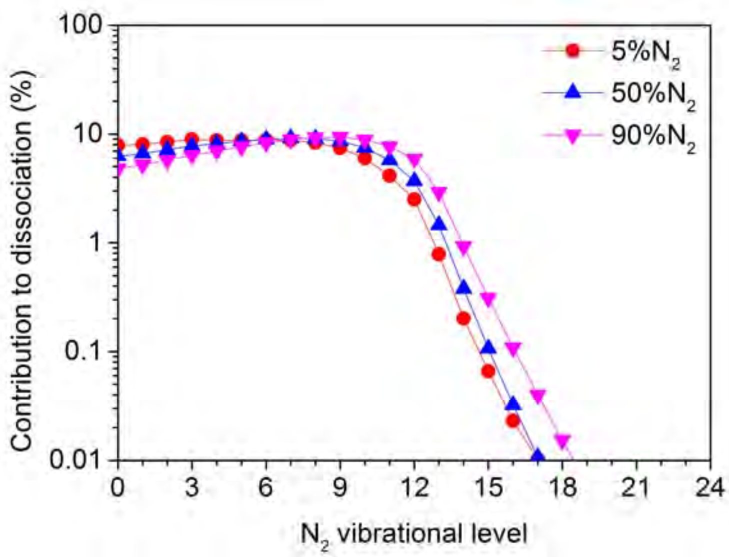

Figure S2. Contribution of the different vibrational levels of N_2 to the total dissociation of N_2 at three different N_2 fractions in the mixture.

The major difference with the sets in 13–15 is that we use the cross section set of Phelps, with the 7 eV threshold excitation reaction used for dissociation, for the electron impact reactions with CO_2 [18–20], as suggested by Grofulovic et al. [21], Bogaerts et al. [22] and Pietanza et al. [23–25]. Furthermore, to account for the high temperature and atmospheric pressure conditions in the GAP, some extra reactions, which become significant at these conditions, are included, and the rate coefficients for some existing reactions are also updated (see Table S2).

Therefore, a large chemistry set (containing 18180 reactions and 134 species, consisting of 14 molecules, 30 charged species, 9 radicals and 81 excited species) is created, including electron impact reactions, electron-ion recombination reactions, ion-ion, ion-neutral and neutral-neutral reactions, as well as vibration-translation (VT) and vibration-vibration (VV) relaxation reactions.

Table S1. Species taken into account in the chemistry set for modeling the GAP.

Molecules	Charged species	Radicals	Excited species
CO_2, CO, N_2, N, NO, N_2O, NO_2, NO_3, N_2O_5, N_2O_3, N_2O_4, C_2N_2	CO_2^+, CO_4^+, CO^+, $C_2O_2^+$, $C_2O_3^+$, $C_2O_4^+$, C_2^+, C^+, CO_3^-, CO_4^-, N^+, N_2^+, N_3^+, N_4^+, NO^+, N_2O^+, NO_2^+, NO^-, N_2O^-, NO_2^-, NO_3^-,$O_2^+N_2$	C_2O, C, C_2, CN, $ONCN$, NCO, NCN, C_2N	CO_2(Va, Vb, Vc, Vd), CO_2(V1-V21), CO_2(E1), CO(V1-V10), CO(E1-E4), N_2(V1-V24), $N_2(C^3\Pi_u)$, $N_2(A^3\Sigma_u)$, $N_2(a^1\Sigma_u)$, $N_2(A^1\Pi_g)$, $N_2(B^3\Pi_g)$, $N_2(W^3\Delta_u)$, $N_2(B^3\Sigma_u)$, $N_2(E^3\Sigma_g)$, $N_2(W^1\Delta_u)$, $N_2(A^1\Sigma_g)$, $N(^2D)$, $N(^2P)$
O_2, O_3	O^+, O_2^+, O_4^+, O^-, O_2^-, O_3^-, O_4^-	O	O_2(V1-V3), O_2(E1-E2)
	electrons		

Table S2. The reactions included in the model are taken from refs. 13–15, but some extra reactions are added, and the rate coefficients of some other reactions are updated, as listed in this table, to account for the high pressure and temperature conditions in the GAP. The rate coefficients are given in $cm^3\ s^{-1}$ and $cm^6\ s^{-1}$ for two-body and three-body reactions, respectively. $\boldsymbol{R}$ is the gas constant and $\boldsymbol{T}$ the gas temperature (in K).

Reaction	**Rate coefficient**	**Reference**
$N + NO \rightarrow N_2 + O$	$1.66x10^{-11}$	26
$N + O_2 \rightarrow O + NO$	$2.36x10^{-11}\exp(-\frac{44.23}{RT})$	27
$O + NO_2 \rightarrow NO + O_2$	$9.05x10^{-12}\left(\frac{T}{298}\right)^{-0.52}$	28
$NO + NO + O_2 \rightarrow NO_2 + NO_2$	$3.30x10^{-39}\exp(\frac{4.41}{RT})$	29
$N_2O + M \rightarrow N_2 + O + M$	$1.20x10^{-9}\exp(-\frac{240.00}{RT})$	30
$NO + O \rightarrow NO_2$	$3.01x10^{-11}\left(\frac{T}{298}\right)^{-0.75}$	31
$NO_2 + M \rightarrow NO + O + M$	$9.40x10^{-5}\left(\frac{T}{298}\right)^{-2.66}\exp(-\frac{311.00}{RT})$	31
$NO_2 + O + CO_2 \rightarrow NO_3 + CO_2$	$6.59x10^{-30}\left(\frac{T}{298}\right)^{-3.94}\exp(-\frac{9.56}{RT})$	31

$NO_2 + O + N_2 \rightarrow NO_3 + N_2$	$3.31x10^{-30}\left(\frac{T}{298}\right)^{-4.08}\exp(-\frac{10.31}{RT})$	31
$N_2O_5 + M \rightarrow NO_2 + NO_3 + M$	$2.10x10^{-11}\left(\frac{T}{300}\right)^{3.50}\exp(-\frac{91.46}{RT})$	32
$CO_2 + NO \rightarrow CO + NO_2$	$(\frac{1}{30})x10^{(-10.59-\left(\frac{32500}{4.58T}\right))}$	33
$C + N_2 \rightarrow CN + N$	$8.70x10^{-11}\exp(-\frac{188.00}{RT})$	34
$C + NO \rightarrow CN + O$	$3.32x10^{-11}$	35
$CN + O \rightarrow CO + N$	$\left(\frac{1}{5}\right)x1.69x10^{-11}$	36
$CO + N \rightarrow CN + O$	$3.84x10^{-9}\exp(-\frac{275.05}{RT})$	37,38
$C_2N_2 + M \rightarrow CN + CN + M$	$3.65x10^{-1}\left(\frac{T}{298}\right)^{-4.32}\exp(-\frac{545.00}{RT})$	39
$CN + NO_2 \rightarrow NO + NCO$	$1.02x10^{-8}(T)^{-0.80}\exp(-\frac{173.63}{T})$	40
$N + NCO \rightarrow CN + NO$	$1.66x10^{-12}$	41
$N + NCO \rightarrow CO + N_2$	$3.30x10^{-11}$	36
$CN + O_2 \rightarrow O + NCO$	$\left(\frac{1}{2.77}\right)1.16x10^{-11}$	42
$O + NCO \rightarrow CN + O_2$	$4.05x10^{-10}\left(\frac{T}{298}\right)^{-1.43}\exp(-\frac{29.10}{RT})$	43
$O + NCO \rightarrow CO + NO$	$7.51x10^{-11}$	43
$CO_2 + CN \rightarrow CO + NCO$	$1.35x10^{-12}\left(\frac{T}{298}\right)^{2.16}\exp(-\frac{112.0}{RT})$	44
$NCO + NO \rightarrow N_2O + CO$	$5.15x10^{-11}\left(\frac{T}{298}\right)^{-1.34}\exp(-\frac{2.99}{RT})$	45
$NCO + NO \rightarrow CO_2 + N_2$	$1.29x10^{-10}\left(\frac{T}{298}\right)^{-1.97}\exp(-\frac{4.66}{RT})$	45
$NCO + NO \rightarrow CO + N_2 + O$	$0.23x1.69x10^{-11}\exp(\frac{1.63}{RT})$	43
$NCO + NO_2 \rightarrow CO + NO + NO$	$1.30x10^{-12}$	46

$NCO + NO_2 \rightarrow CO_2 + N_2O$	$5.40x10^{-12}\exp(\frac{354.81}{T})$	40
$NCO + NCO \rightarrow N_2 + CO + CO$	$3.01x10^{-11}$	43
$NCO + M \rightarrow N + CO + M$	$1.69x10^{-9}\exp(-\frac{195.0}{RT})$	36
$N_2O + NCO \rightarrow CO + N_2 + NO$	$1.50x10^{-10}\exp(-\frac{116.0}{RT})$	43
$NCN + O \rightarrow N + NCO$	$4.02x10^{-14}\left(\frac{T}{298}\right)^{0.42}\exp(\frac{0.66}{RT})$	47
$NCN + O \rightarrow N_2 + CO$	$2.22x10^{-16}\left(\frac{T}{298}\right)^{2.32}\exp(\frac{4.75}{RT})$	47
$NCN + O \rightarrow CN + NO$	$1.54x10^{-10}\exp(-\frac{5.80}{RT})$	48
$NCN + NO \rightarrow CN + N_2O$	$3.16x10^{-12}\exp(-\frac{26.30}{RT})$	49
$NCN + O_2 \rightarrow NO + NCO$	$1.15x10^{-13}\left(\frac{T}{298}\right)^{0.51}\exp(-\frac{103.00}{RT})$	50
$NCN + NCN \rightarrow CN + CN + N_2$	$6.14x10^{-12}$	48
$NCN + M \rightarrow C + N_2 + M$	$1.48x10^{-9}\exp(-\frac{260.00}{RT})$	48
$NO + NO_2 + M \rightarrow N_2O_3 + M$	$3.09x10^{-34}\left(\frac{T}{298}\right)^{-7.70}$	32
$N_2O_3 + M \rightarrow NO + NO_2 + M$	$1.91x10^{-7}\left(\frac{T}{298}\right)^{-8.70}\exp(-\frac{40.57}{RT})$	32
$NO_2 + NO_2 + M \rightarrow N_2O_4 + M$	$1.40x10^{-33}\left(\frac{T}{298}\right)^{-3.80}$	32
$N_2O_4 + M \rightarrow NO_2 + NO_2 + M$	$1.30x10^{-5}\left(\frac{T}{298}\right)^{-3.80}\exp(-\frac{53.21}{RT})$	32
$CO_2 + N \rightarrow CO + NO$	$5.00x10^{-16}$	51
$CO_2 + N(^2D) \rightarrow CO + NO$	$3.60x10^{-13}$	52
$CO + N_2O \rightarrow CO_2 + N_2$	$5.30x10^{-13}\exp(-\frac{84.81}{RT})$	31

$NO_3 + O_3 \rightarrow NO_2 + O_2 + O_2$	$1.00x10^{-17}$	53
$CO + M \rightarrow C + O + M$	$1.52x10^{-4}\left(\frac{T}{298}\right)^{-3.10}\exp(-\frac{1073.00}{RT})$	54
$C + NO \rightarrow CO + N$	$4.82x10^{-11}$	55
$CN + NO_2 \rightarrow CO + N_2O$	$0.08x5.01x10^{-11}\exp(\frac{1.42}{RT})$	56
$CN + NO_2 \rightarrow CO_2 + N_2$	$0.06x5.01x10^{-11}\exp(\frac{1.42}{RT})$	56
$N + CN + M \rightarrow NCN + M$	$2.76x10^{-32}$	57
$CN + N_2O \rightarrow NCN + NO$	$1.73x10^{-14}\left(\frac{T}{298}\right)^{2.60}\exp(-\frac{15.46}{RT})$	43
$NCN + NO_2 \rightarrow ONCN + NO$	$7.80x10^{-12}\exp(-\frac{38.00}{RT})$	49
$C_2N_2 + O \rightarrow CN + NCO$	$4.15x10^{-11}\exp(-\frac{45.73}{RT})$	58
$C_2N_2 + O \rightarrow NCN + CO$	$2.31x10^{-10}\exp(-\frac{7540.00}{T})$	59
$C_2N + N \rightarrow CN + CN$	$1.0x10^{-10}$	60
$C_2N + O \rightarrow CN + CO$	$5.99x10^{-12}$	61
$C_2 + NO \rightarrow C_2N + O$	$0.70x1.25x10^{-10}\exp(-\frac{36.17}{RT})$	62
$C_2N_2 + C \rightarrow CN + C_2N$	$3.01x10^{-11}$	60
$C_2N_2 + N \rightarrow C_2N + N_2$	$4.98x10^{-8}\exp(-\frac{17500.00}{T})$	63
$N_2O_5 + O \rightarrow N_2 + O_2 + O_2 + O_2$	$3.00x10^{-16}\left(\frac{T}{300}\right)^{0.50}$	64
$CN + NO \rightarrow NCN + O$	$2.99x10^{-11}\exp(-\frac{19220.00}{T})$	65
$CN + NCN \rightarrow N + C_2N_2$	$3.32x10^{-11}$	65
$N + NCN \rightarrow N_2 + CN$	$1.66x10^{-11}$	65
$NCN + M \rightarrow N + CN + M$	$8.47x10^{-9}\exp(-\frac{53300.00}{T})$	65
$C + NCN \rightarrow CN + CN$	$1.66x10^{-11}$	65

C + NCO → CN + CO	$1.66x10^{-11}$	65
NCN + NCO → CN + N_2 + CO	$1.66x10^{-11}$	65

Results and discussion

CO_2 conversion, energy cost and energy efficiency

Table S3. Concentrations, as well as the carbon and oxygen balance. Note that the C-balance is always lower and the O-balance is always higher than 100 %, which can be explained by the accuracy of the calibration method within the gas chromatograph.

IN (%)		OUT (%)				OUT (ppm)		C-balance (%)	O-balance (%)
CO_2	N_2	CO_2	N_2	CO	O_2	NO	NO_2		
99.53	0.08	92.04	0.04	5.71	2.90	0	0	98.21	101.12
94.50	5.33	85.69	5.10	6.27	3.07	1023.1	9.60	97.31	100.56
89.82	10.33	82.28	10.05	6.24	3.01	3178	54.6	98.56	101.90
80.39	20.46	72.24	19.88	5.94	2.78	5545	170.1	97.26	100.72
69.37	30.59	63.21	29.94	5.79	2.65	6408	264.6	99.47	103.29
59.99	40.60	53.44	39.67	5.64	2.52	6453	307.3	98.50	102.71
50.46	50.63	44.32	49.68	5.21	2.25	5998	316.9	98.15	102.60
40.29	60.76	35.28	59.82	4.63	1.99	5275	286	99.06	103.99
30.31	70.89	25.99	70.17	3.86	1.62	4507	241	98.49	103.83
19.74	80.42	16.37	80.18	2.92	1.21	3620	201.3	97.76	103.91
9.20	89.45	7.34	89.70	1.73	0.72	2136	143.5	98.63	106.49
3.79	94.61	2.80	95.12	0.96	0.44	1524.4	108.17	99.15	110.79

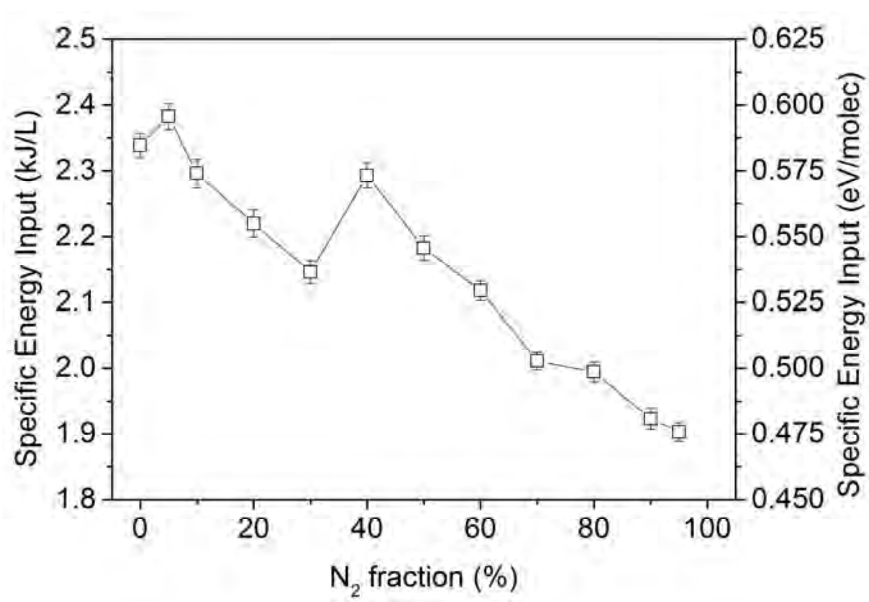

Figure S3. There is a small drop in specific energy input (SEI) upon N_2 addition.

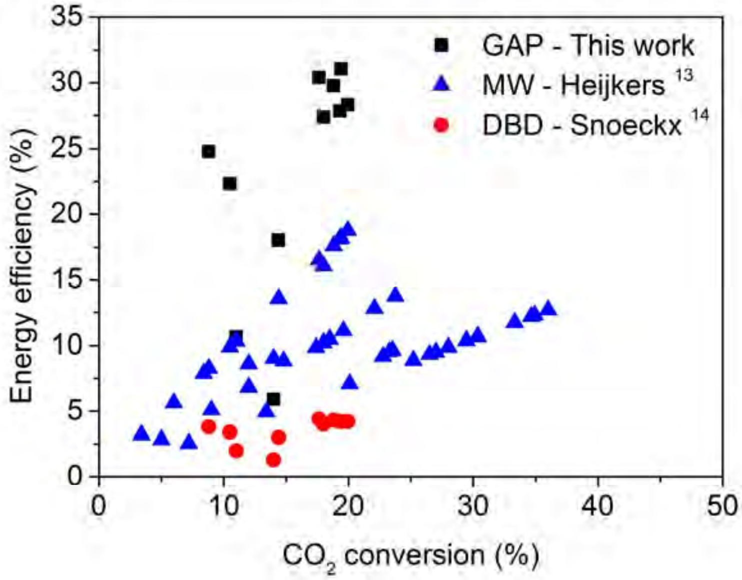

Figure S4. Comparison of the energy efficiency versus CO_2 conversion in three different types of plasma reactors mostly studied for CO_2 conversion: gliding arc plasmatron (GAP; this work), microwave plasma (MW; Heijkers[13]) and dielectric barrier discharge (DBD; Snoeckx[14]).

In general, most studies for CO_2 conversion are carried out in these three plasma types[66], but studies with addition of N_2 are still limited to these two references and our current work.

Analysis of the byproducts - NOx concentrations

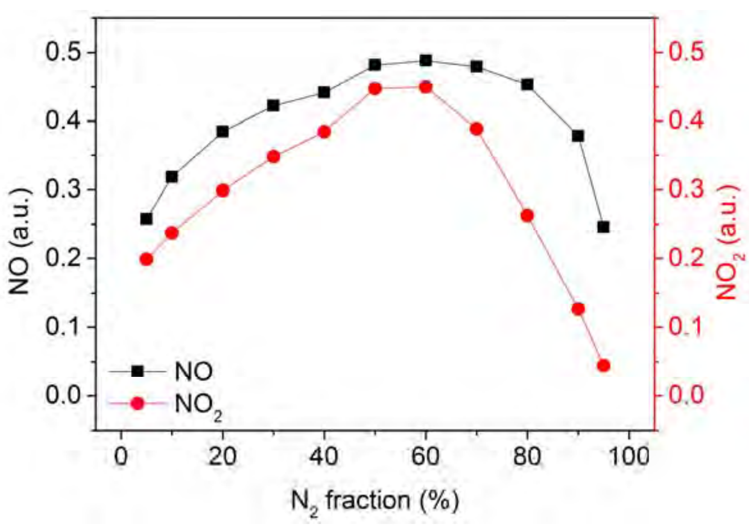

Figure S5. NO and NO_2 concentration in arbitrary units as a function of N_2 fraction, as obtained from the FTIR measurements.

Table S4. NO and NO_2 concentration and calculated error, in parts per million, as obtained from the QCL measurements.

N_2 fraction (%)	NO (ppm)		NO_2 (ppm)	
	Value	Error	Value	Error
5	1524.4	0.8	108.17	0.09
10	2136	1	143.5	0.2
20	3620	8	201.3	0.4
30	4507	19	241	1
40	5275	21	286	1
50	5998	8	316.9	0.5
60	6453	14	307.3	0.7
70	6408	10	264.6	0.4
80	5545	9	170.1	0.3
90	3178	7	54.6	0.1
95	1023.1	0.3	9.60	0.02

The maximum total NOx concentration obtained is 6761 ppm at 60 % N_2. To make the process effective for N_2 fixation, the NOx concentration should be above 1%, as stated in the main paper. For this purpose, we should enhance the CO_2 conversion in the GAP. To realize the latter, the fraction of gas passing through the arc should be increased to 22%. This can be explained as follows: from previous fluid dynamics calculations we know that the fraction of gas passing through the arc is 14.8 % [7] (used in equation 20). Based on this number, we calculated that the conversion inside the arc is about 71 % (equation 21).

$$X_{CO_2}^{Absolute}(\%) = X_{CO_2,arc}(\%) \times 0.148 \tag{20}$$

$$X_{CO_2,arc}(\%) = \frac{X_{CO_2}^{Absolute}(\%)}{0.148} = \frac{10.5\ \%}{0.148} = 71\ \% \tag{21}$$

As we now obtain a maximum NOx concentration of 6761 ppm at 60 % N_2, and when this must be increased up to 1 %, we need an increase of $X_{CO_2}^{Absolute}$ up to 16 %. Assuming that we have 71 % CO_2 conversion in the arc and we need an absolute CO_2 conversion of 16 %, we need a fraction of 22 % passing through the arc (equation 22).

$$fraction_{arc} = \frac{X_{CO_2}^{Absolute}(\%)}{X_{CO_2,arc}(\%)} = \frac{16\ \%}{71\ \%} = 0.22 \tag{22}$$

Underlying mechanisms as revealed by computer simulations

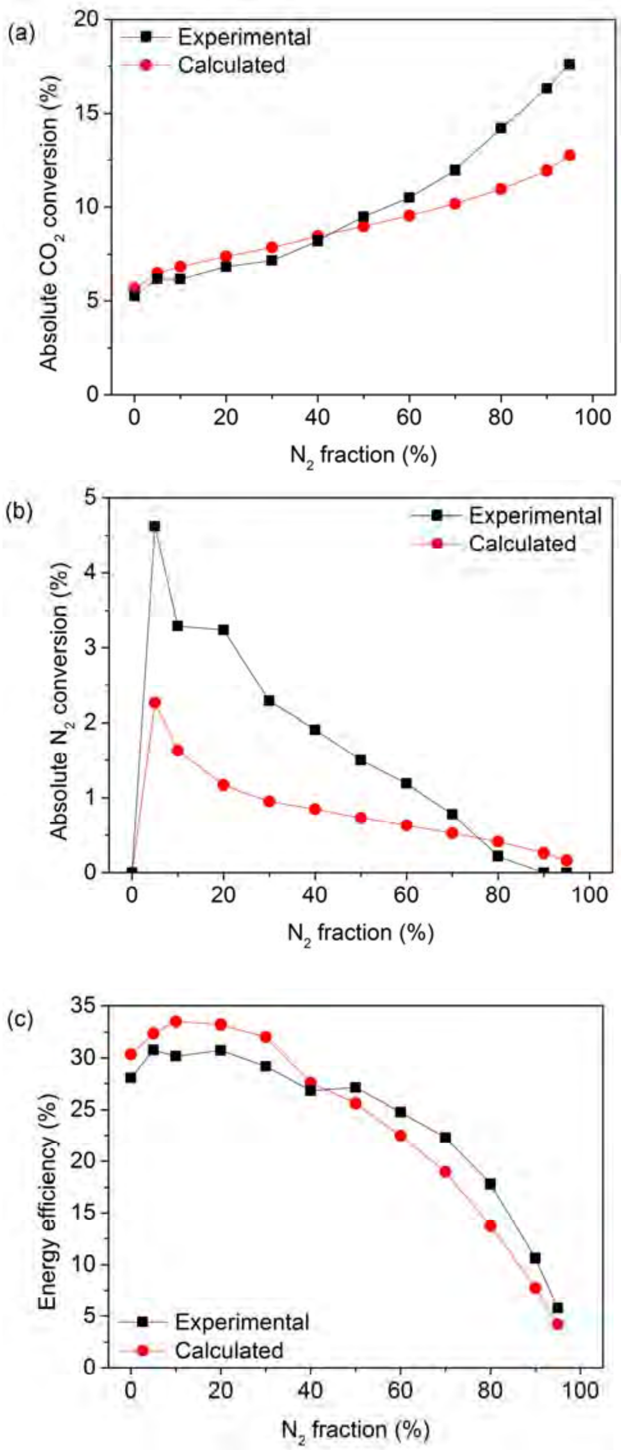

Figure S6. Experimental and calculated results for CO_2 conversion (a), N_2 conversion (b) and energy efficiency (c).

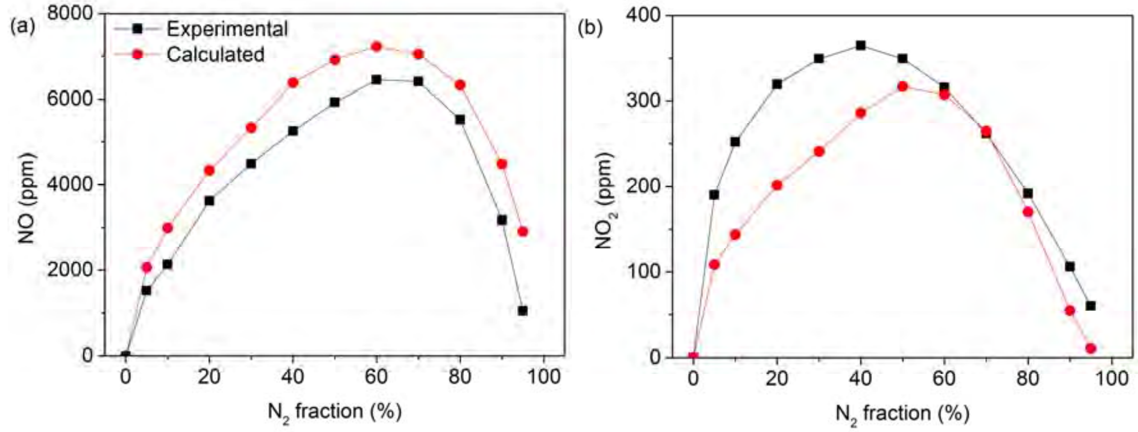

Figure S7. Experimental and calculated results for NO (a) and NO_2 (b) concentration (in parts per million).

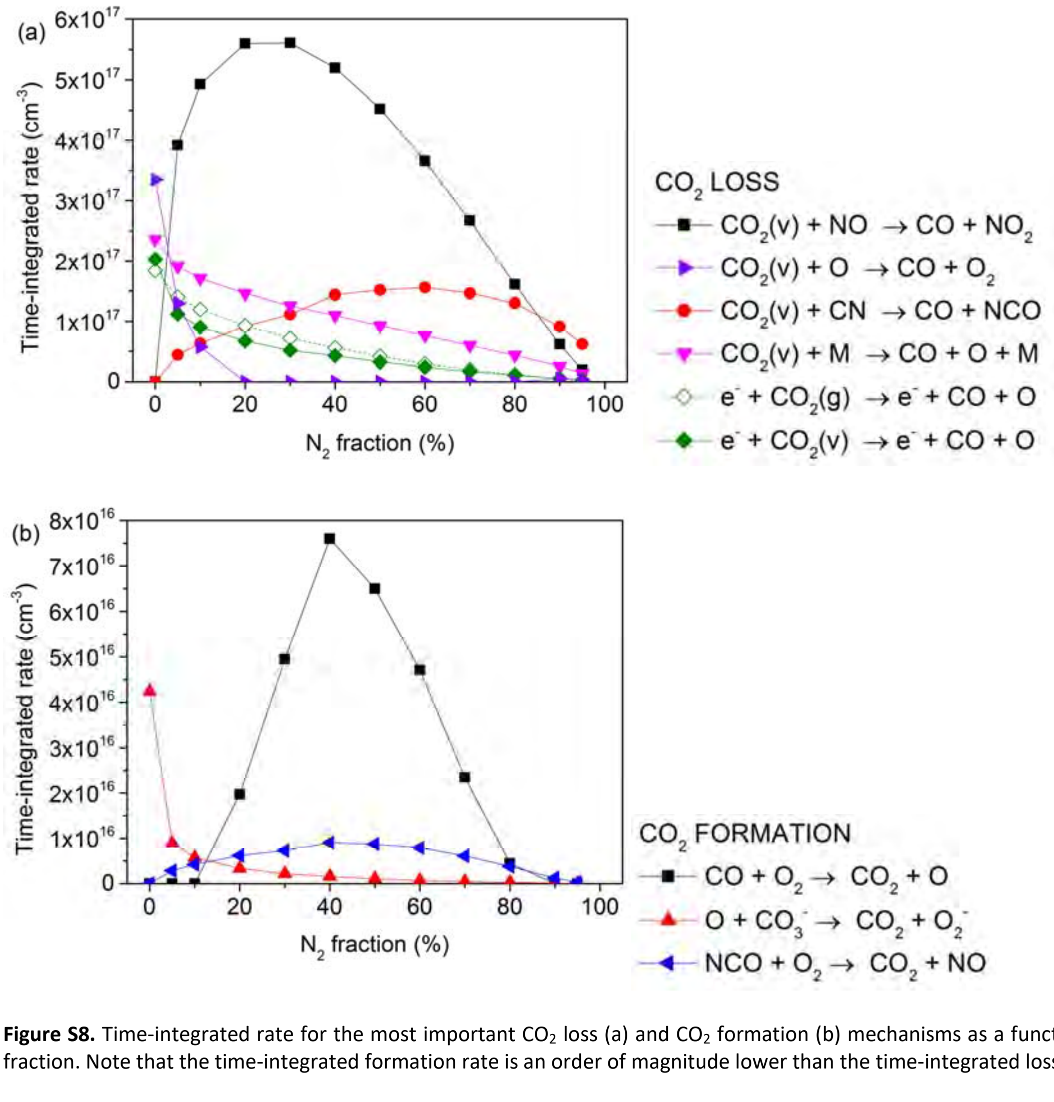

Figure S8. Time-integrated rate for the most important CO_2 loss (a) and CO_2 formation (b) mechanisms as a function of N_2 fraction. Note that the time-integrated formation rate is an order of magnitude lower than the time-integrated loss rate.

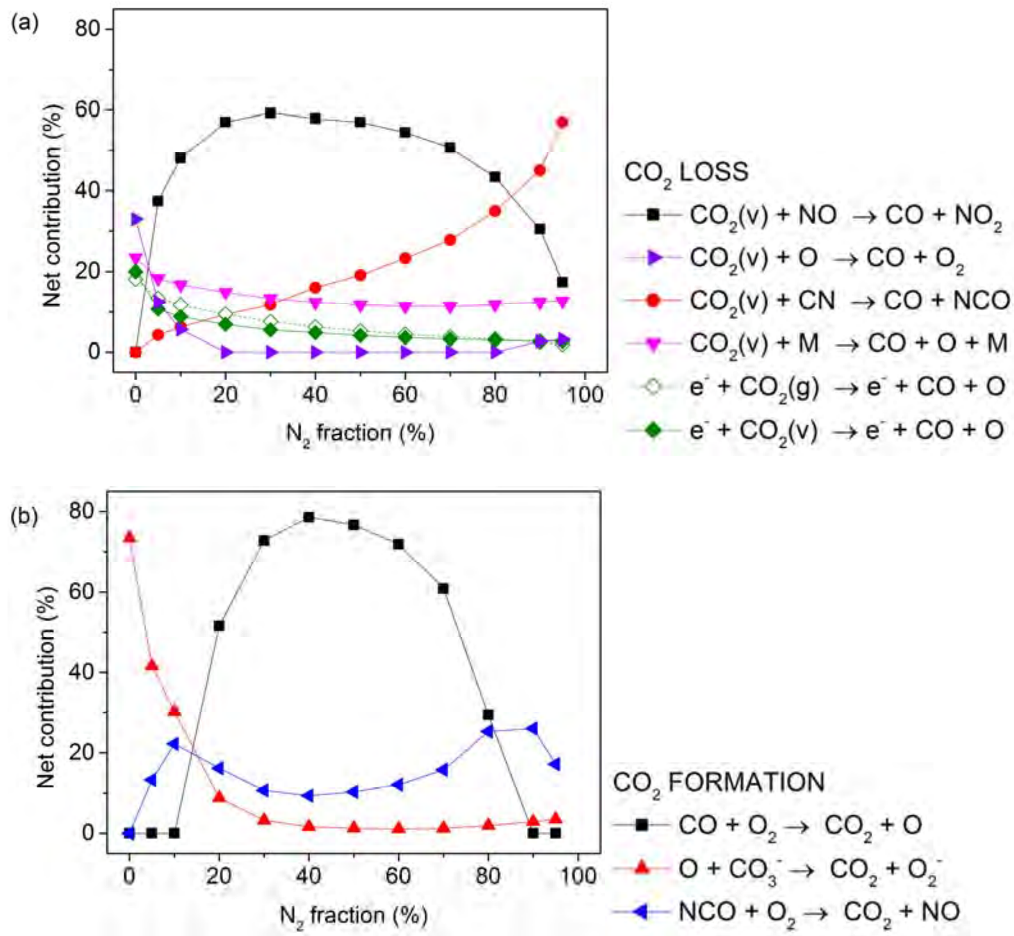

Figure S9. Net contribution of the most important loss (a) and formation (b) reactions of CO_2.

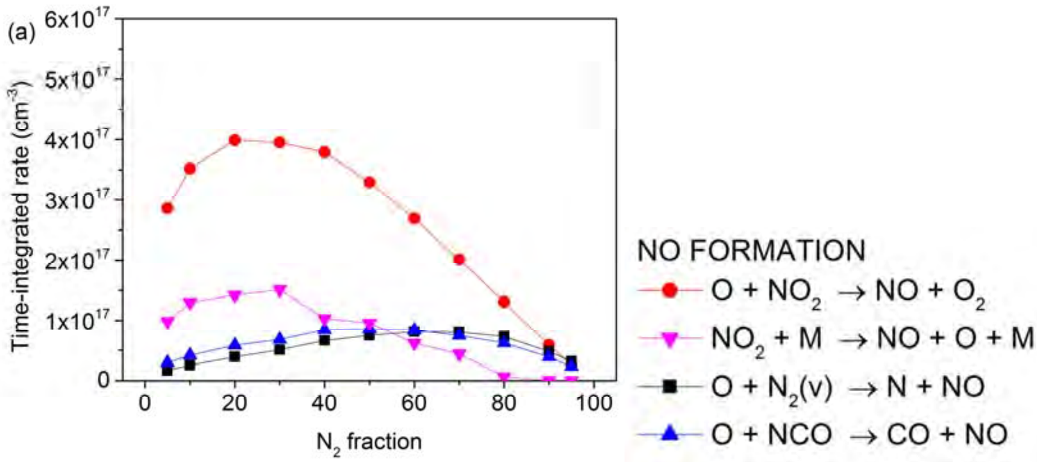

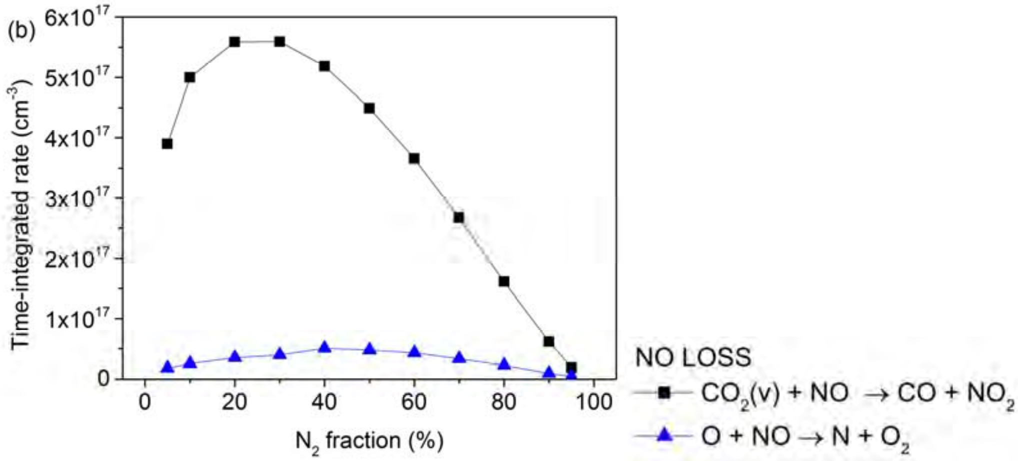

Figure S10. Time-integrated rate for the most important NO formation (a) and NO loss (b) mechanisms as a function of N_2 fraction.

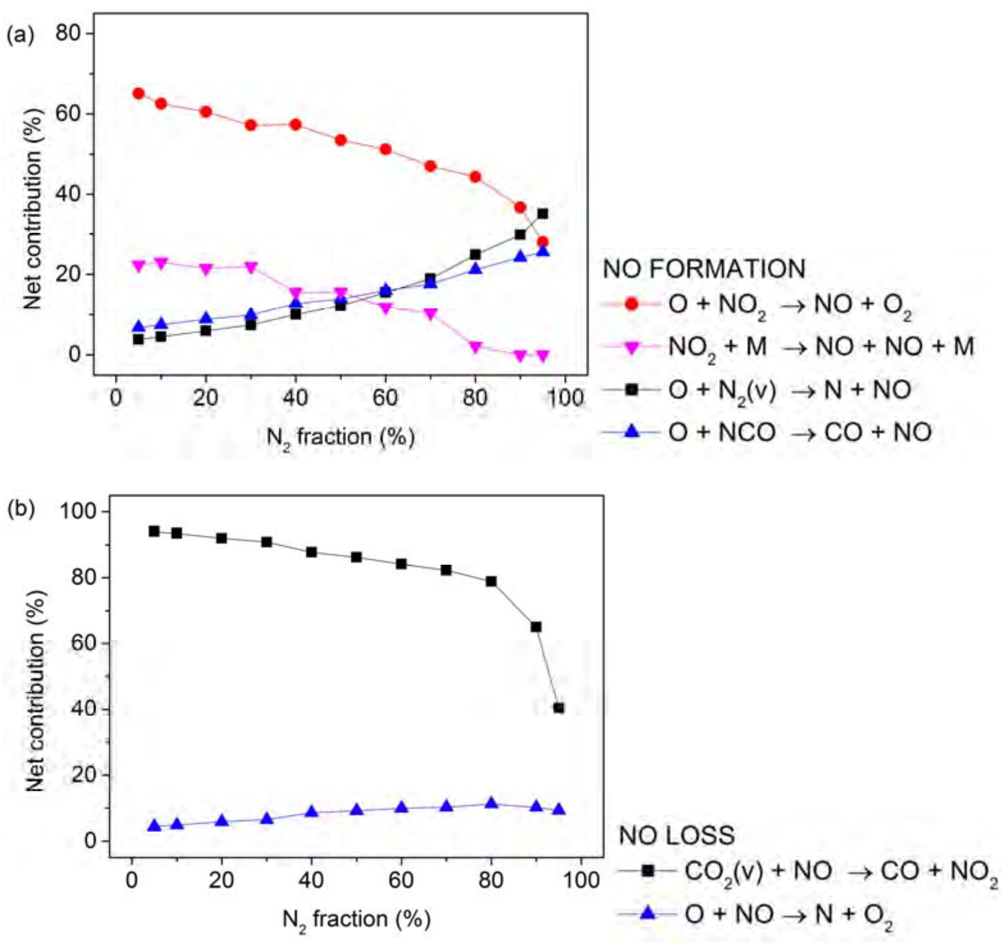

Figure S11. Net contribution of the most important formation (a) and loss (b) reactions of NO.

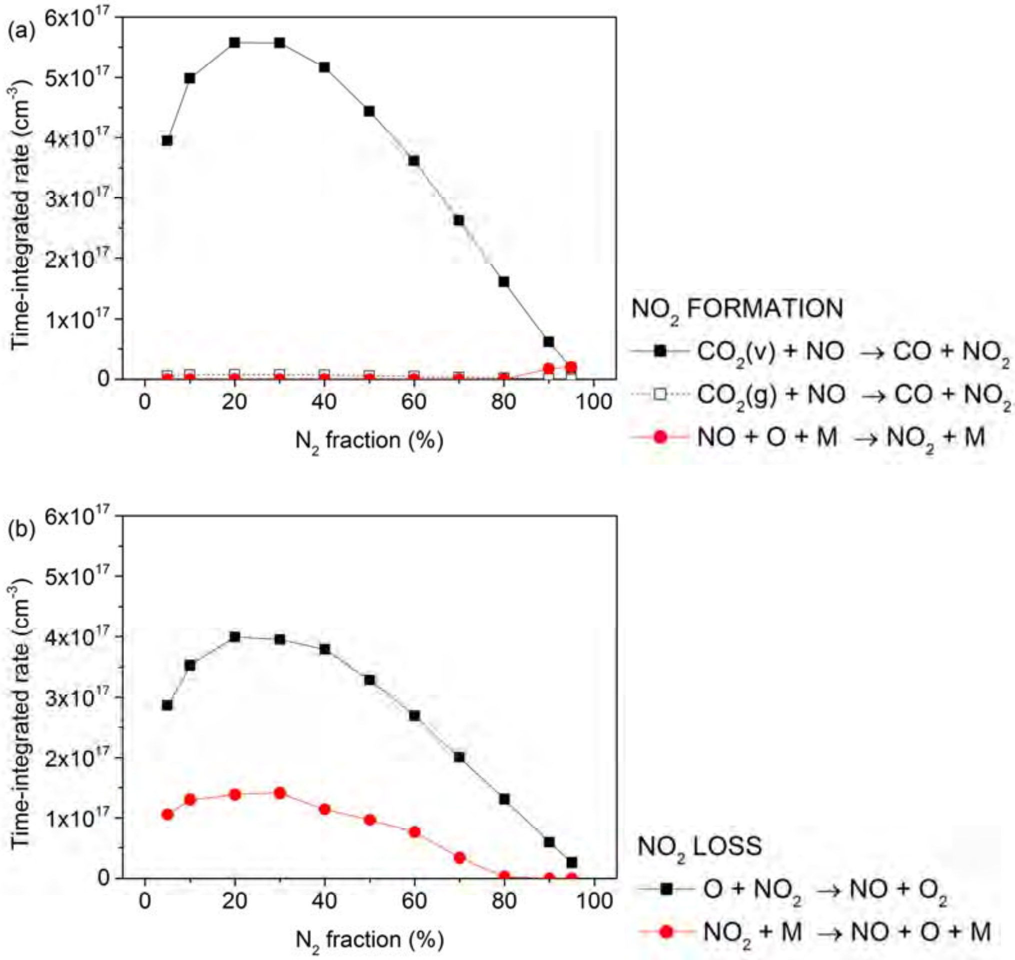

Figure S12. Time-integrated rate for the most important NO_2 formation (a) and NO_2 loss (b) mechanisms as a function of N_2 fraction.

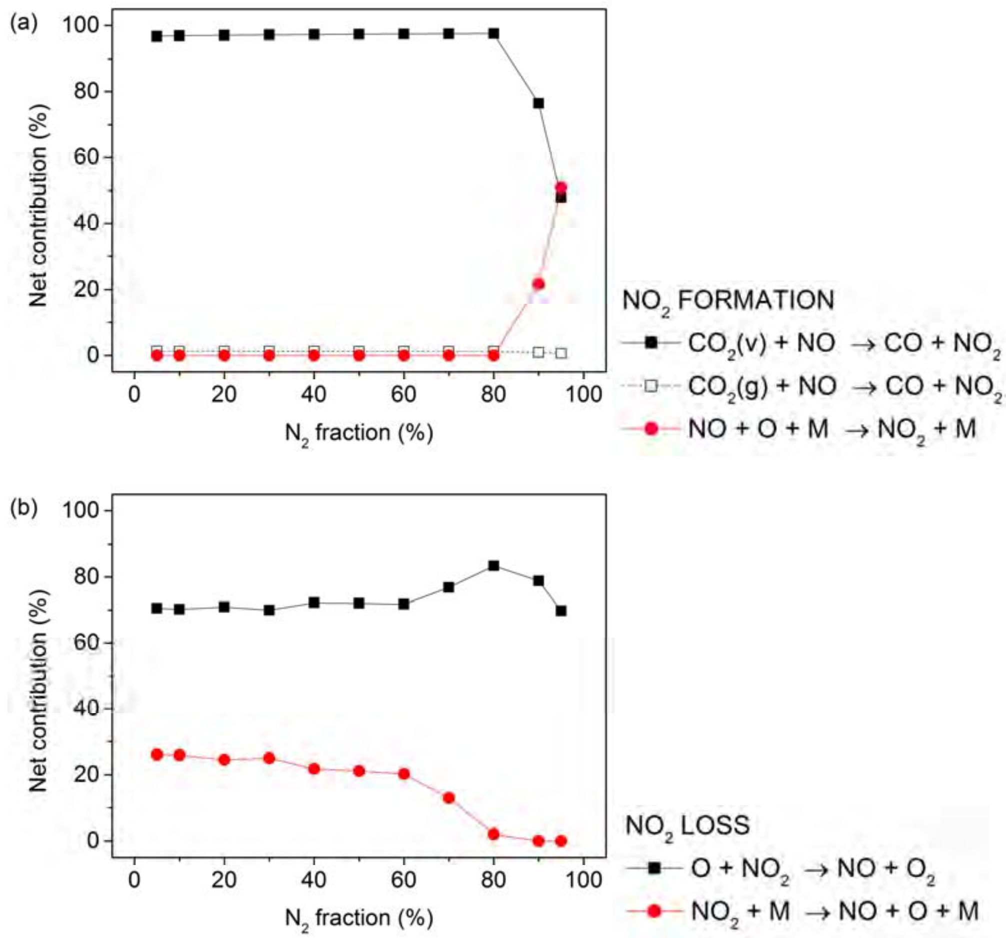

Figure S13. Net contribution of the most important formation (a) and loss (b) reactions of NO_2.

Table S5. Most important reactions, ranked by importance based on the average time-integrated rate.

Reactions	**Average time-integrated rate (cm^{-3})**
$CO_2 + NO \rightarrow CO + NO_2$	3.55×10^{17}
$O + NO_2 \rightarrow NO + O2$	2.57×10^{17}
$CO + N \rightarrow CN + O$	1.38×10^{17}
$e^- + CO2 \rightarrow e^- + CO + O$	1.19×10^{17}
$CO_2 + M \rightarrow CO + O + M$	1.16×10^{17}
$CO_2 + CN \rightarrow CO + NCO$	1.15×10^{17}
$NO_2 + M \rightarrow NO + O + M$	7.63×10^{16}
$NCO + M \rightarrow N + CO + M$	5.96×10^{16}
$O + N_2 \rightarrow N + NO$	5.93×10^{16}
$O + NCO \rightarrow CO + NO$	5.92×10^{16}
$CO + O_2 \rightarrow CO_2 + O$	3.17×10^{16}
$NCO + NO \rightarrow CO + N_2 + O$	6.61×10^{15}
$N_2O + M \rightarrow N_2 + O + M$	6.49×10^{15}
$N + NO_2 \rightarrow N_2O + O$	3.78×10^{15}
$NCO + NO \rightarrow N_2O + CO$	3.13×10^{15}
$NO_2 + NO_3 + M \rightarrow N_2O_5 + M$	6.88×10^{13}
$NO_2 + NO_2 + M \rightarrow N_2O_4 + M$	9.34×10^{8}
$NO + NO_2 + M \rightarrow N_2O_3 + M$	4.28×10^{7}

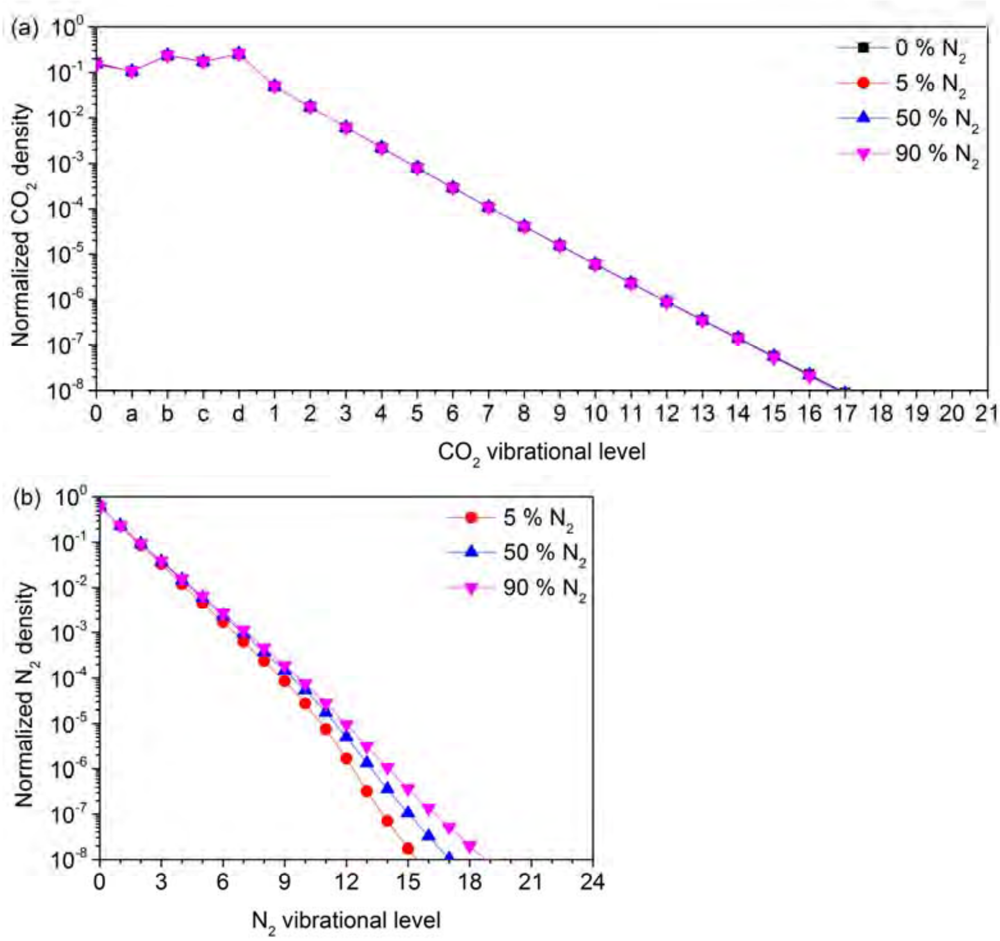

Figure S14. The calculated vibrational distribution of CO_2 (a) and N_2 (b) are nearly thermal, in the entire range of N_2 fractions in the mixture.

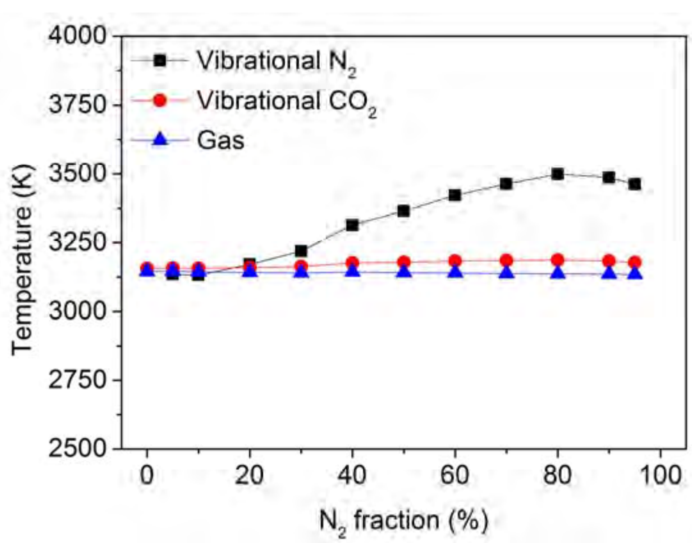

Figure S15. The average gas temperature is 3140 K, while the average vibrational temperature of CO_2 and N_2 are 3174 K and 3333 K, respectively.

Comparison of gliding arc plasmatron with dielectric barrier discharge

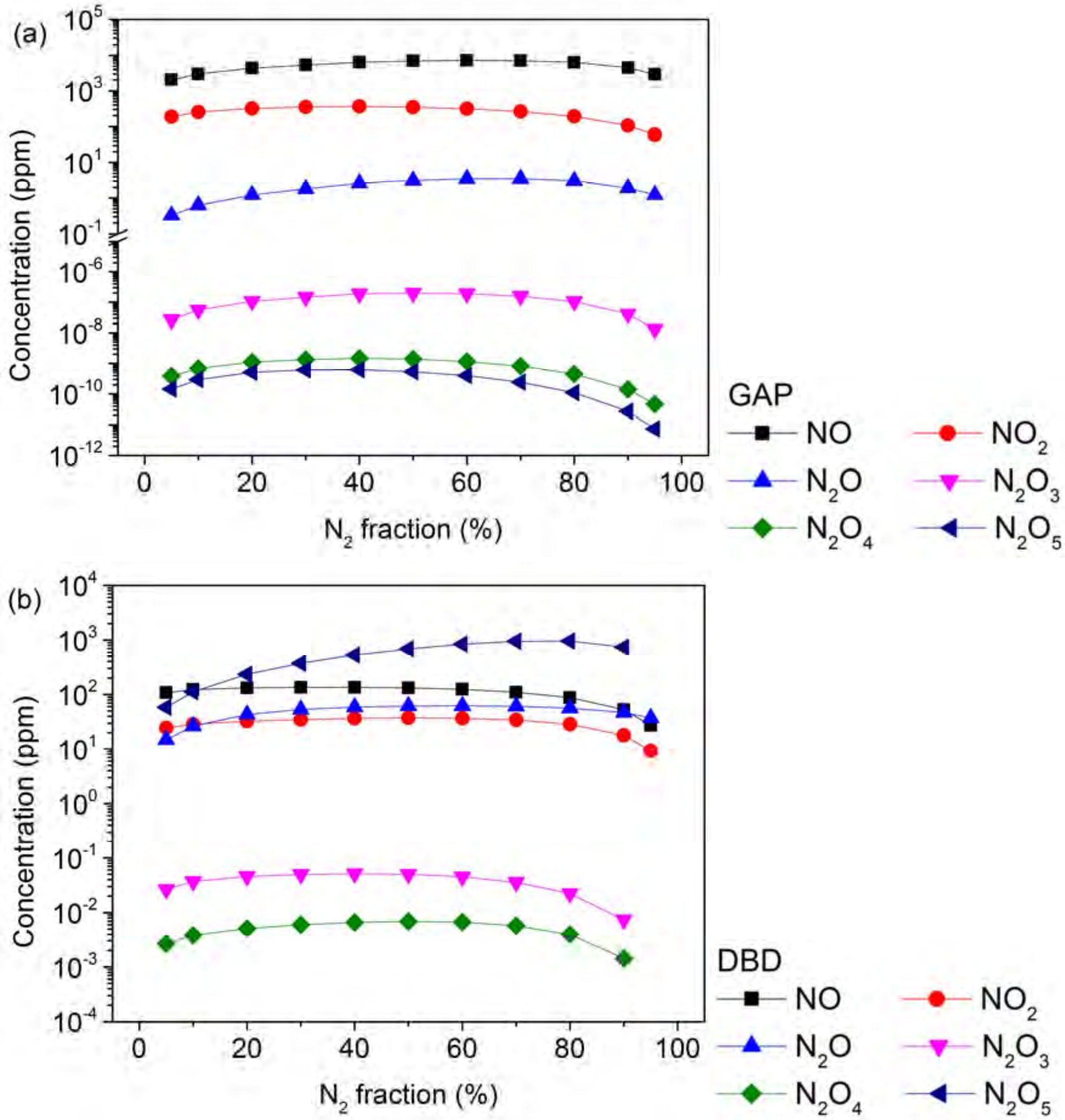

Figure S16. Concentration of the most important byproducts in the GAP (a) and DBD (b) as a function of N_2 fraction, obtained by modeling.

In Figure S17, we plot the total time-integrated net formation (a) and loss (b) rates of N_2O, N_2O_3, N_2O_4 and N_2O_5, in both a GAP and DBD. It is clear that the total formation rate is lower than the total loss rate in the GAP, while it is higher in the DBD, explaining why these species have a much higher concentration in the DBD than in the GAP.

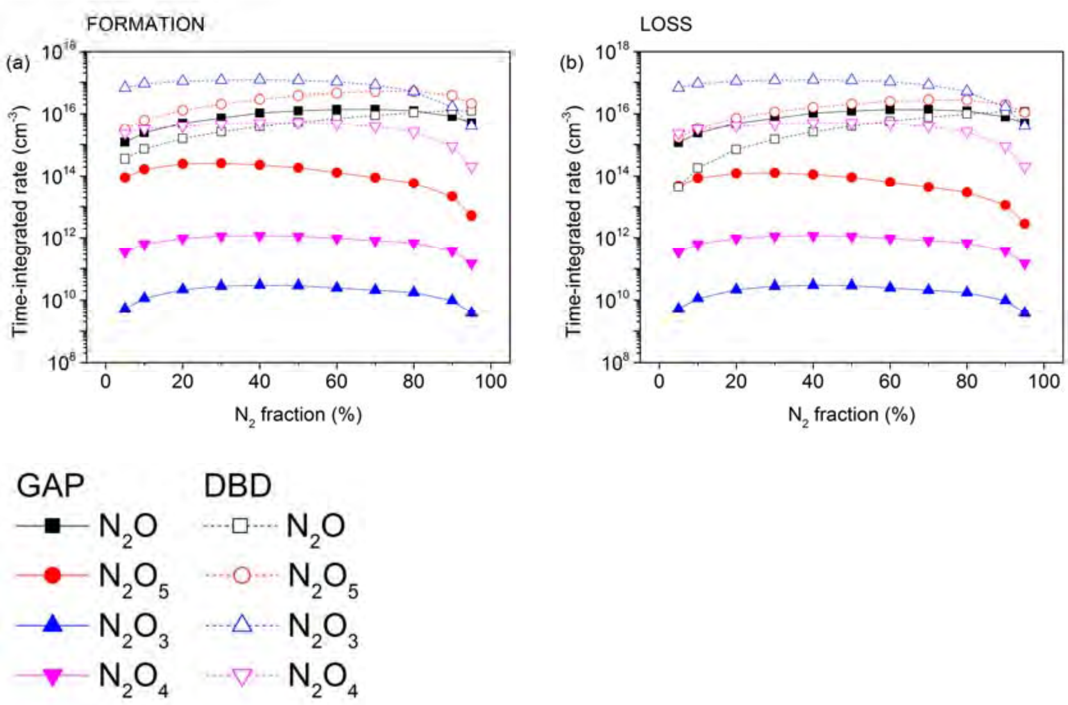

Figure S17. Total time-integrated net formation (a) and loss (b) rates of N_2O, N_2O_3, N_2O_4, N_2O_5, in both a GAP and DBD.

References

1 M. Ramakers, G. Trenchev, S. Heijkers, W. Wang and A. Bogaerts, *Chem. Sus. Chem.*, 2017, **10**, 2642–2652.

2 S. Pancheshnyi, B. Eismann, G. J. M. Hagelaar and L. C. Pitchford, 2008, University of Toulouse, LAPLACE, CNRS-UPS-INP.

3 G. J. M. Hagelaar and L. C. Pitchford, *Plasma Sources Sci. Technol.*, 2005, **14**, 722–733.

4 M. A. Lieberman and A. J. Lichtenberg, *Principles of Plasma Discharges and Materials Processing: Second Edition*, Wiley-Interscience, 2nd Editio., 2005.

5 G. Trenchev, S. Kolev, W. Wang, M. Ramakers and A. Bogaerts, *J. Phys. Chem. C*, 2017, **121**, 24470–24479.

6 T. P. Nunnally, PhD Thesis, Drexel University, 2011.

7 E. Cleiren, S. Heijkers, M. Ramakers and A. Bogaerts, *Chem. Sus. Chem.*, 2017, **10**, 4025–4036.

8 S. Heijkers and A. Bogaerts, *J. Phys. Chem. C*, 2017, **121**, 22644–22655.

9 T. Kozak and A. Bogaerts, *Plasma Sources Sci. Technol.*, 2015, **24**, 015024.

10 W. Wang, A. Berthelot, S. Kolev, X. Tu and A. Bogaerts, *Plasma Sources Sci. Technol.*, 2016, **25**, 065012.

11 M. Chase, *J. Phys. Chem. Ref. Data, Monogr. 9*, 1998, 1952.

12 G. Trenchev, S. Kolev and A. Bogaerts, *Plasma Sources Sci. Technol.*, 2016, **25**, 035014.

13 S. Heijkers, R. Snoeckx, T. Kozak, T. Silva, T. Godfroid, N. Britun, R. Snyders and A. Bogaerts, *J. Phys. Chem. C*, 2015, **119**, 12815–12828.

14 R. Snoeckx, S. Heijkers, K. Van Wesenbeeck, S. Lenaerts and A. Bogaerts, *Energy Environ. Sci.*, 2016, **9**, 30–39.

15 W. Wang, B. Patil, S. Heijkers, V. Hessel and A. Bogaerts, *ChemSusChem*, 2017, **10**, 2145–2157.

16 T. Kozák and A. Bogaerts, *Plasma Sources Sci. Technol.*, 2014, **23**, 045004.

17 A. Fridman, *Plasma Chemistry*, Cambridge University Press, New York, U.S.A., 2008.

18 A. V. Phelps, Phelps Database www.lxcat.net.

19 J. J. Lowke, A. V. Phelps and B. W. Irwin, *J. Appl. Phys.*, 1973, **44**, 4664–4671.

20 R. D. Hake and A. V. Phelps, *Phys. Rev.*, 1967, **158**, 70–84.

21 M. Grofulovic, L. L. Alves and V. Guerra, *J. Phys. D Appl. Phys.*, 2016, **49**, 395207.

22 A. Bogaerts, W. Wang, A. Berthelot and V. Guerra, *Plasma Sources Sci. Technol.*, 2016, **25**, 055016.

23 L. D. Pietanza, G. Colonna, G. D'Ammando, A. Laricchiuta and M. Capitelli, *Plasma Sources Sci. Technol.*, 2015, **24**, 042002.

24 L. D. Pietanza, G. Colonna, G. D'Ammando, A. Laricchiuta and M. Capitelli, *Phys. Plasmas*, 2016, **23**, 013515.

25 L. D. Pietanza, G. Colonna, G. D'Ammando, A. Laricchiuta and M. Capitelli, *Chem. Phys.*, 2016, **468**, 44–52.

26 M. Koshi, M. Yoshimura, K. Fukuda, H. Matsui, K. Saito, M. Watanabe, A. Imamura and C. Chen, *J. Chem. Phys.*, 1990, **93**, 8703–8708.

27 G. Suzzi Valli, R. Orrú, E. Clementi, A. Laganà and S. Crocchianti, *J. Chem. Phys.*, 1995, **102**, 2825–2832.

28 P. P. Bemand, M. A. A. Clyne and R. T. Watson, *J. Chem. Soc., Faraday Trans. 2*, 1974, **70**, 564–576.

29 R. Atkinson, D. L. Baulch, R. a. Cox, J. N. Crowley, R. F. Hampson, R. G. Hynes, M. E. Jenkin, M. J. Rossi and J. Troe, *Atmos. Chem. Phys.*, 2004, **4**, 1461–1738.

30 S. Javoy, R. Mevel and C. E. Paillard, *Int. J. Chem. Kinet.*, 2009, **41**, 357–375.

31 W. Tsang and J. T. Herron, *J. Phys. Chem. Ref. Data*, 1991, 20, 609–663.

32 R. Atkinson, D. L. Baulch, R. A. Cox, R. F. Hampson Jr., J. A. Kerr, M. J. Rossi and J. Troe, *J. Phys. Chem. Ref. Data*, 1997, **26**, 1329–1499.

33 T. C. Clark, S. H. Garnett and G. B. Kistiakowsky, *J. Chem. Phys.*, 1969, **51**, 2885–2891.

34 D. L. Baulch, C. J. Cobos, R. A. Cox, P. Frank, G. Hayman, T. Just, J. A. Kerr, T. Murrells, M. J. Pilling, J. Troe, R. W. Walker and J. Warnatz, *J. Phys. Chem. Ref. Data*, 1994, **23**, 847–1033.

35 A. J. Dean, D. F. Davidson and R. K. Hanson, *J. Phys. Chem.*, 1991, **95**, 183–191.

36 D. L. Baulch, C. J. Cobos, R. A. Cox, C. Esser, P. Frank, T. Just, J. A. Kerr, M. J. Pilling, J. Troe, R. W. Walker and J. Warnatz, *J. Phys. Chem. Ref. Data*, 1992, **21**, 411–734.

37 L. B. Ibragimova, *Recommended Values of the Rate Constants of Gas-Phase Chemical Reactions in the N-C-O Atom System. I. Reactions Involving CN, NO, and N_2 Molecules. Preprint No.29-97*, Moscow State University, Institute of Mechanics, 1997.

38 L. B. Ibragimova, *Recommended Values of the Rate Constants of Gas-Phase Chemical Reactions in the N-C-O Atom System. II. Reactions Involving CO_2 and CO Molecules. Preprint No.30-97*, Moscow State University, Institute of Mechanics, 1997.

39 K. Natarajan, K. Thielen, H. D. Hermanns and P. Roth, *Ber. Bunsenges. Phys. Chem.*, 1986, **90**, 533–539.

40 S. T. Wooldridge, J. D. Mertens, R. K. Hanson and C. T. Bowman, in *Twenty-Fifth Symposium (International) on Combustion/The Combustion Institute*, 1994, pp. 983–991.

41 A. Lifshitz and M. Frenklach, *Int. J. Chem. Kinet.*, 1980, **12**, 159–168.

42 M. Burmeister, S. K. Gulati, K. Natarajan, K. Thielen, E. Mozzhukin and P. Roth, *Symp. Int. Combust. Proc.*, 1989, **22**, 1083–1092.

43 W. Tsang, *J. Phys. Chem. Ref. Data*, 1992, **21**, 753–791.

44 N. S. Wang, D. L. Yang, M. C. Lin and C. F. Melius, *Int. J. Chem. Kinet.*, 1991, **23**, 151–160.

45 M. C. Lin, Y. He and C. F. Melius, *J. Phys. Chem.*, 1993, **97**, 9124–9128.

46 J. Park and J. F. Hershberger, *J. Phys. Chem.*, 1993, **97**, 13647–13652.

47 R. S. Zhu and M. C. Lin, *J. Phys. Chem. A*, 2007, **111**, 6766–6771.

48 J. Dammeier, N. Faßheber and G. Friedrichs, *Phys. Chem. Chem. Phys.*, 2012, **14**, 1030–1037.

49 J. Dammeier and G. Friedrichs, *J. Phys. Chem. A*, 2011, **115**, 14382–14390.

50 R. S. Zhu and M. C. Lin, *Int. J. Chem. Kinet.*, 2005, **37**, 593–598.

51 A. Fernandez, A. Goumri and A. Fontijn, *J. Phys. Chem. A*, 1998, **102**, 168–172.

52 J. T. Herron, *J. Phys. Chem. Ref. Data*, 1999, **28**, 1453–1483.

53 J. Hjorth, J. Notholt and G. Restelli, *Int. J. Chem. Kinet.*, 1992, **24**, 51–65.

54 H. Mick, M. Burmeister and P. Roth, *AIAA J.*, 1993, **31**, 671–676.

55 A. J. Dean, R. K. Hanson and C. T. Bowman, *J. Phys. Chem.*, 1991, **95**, 3180–3189.

56 J. Park and J. F. Hershberger, *J. Chem. Phys.*, 1993, **99**, 3488–3493.

57 G. M. Provencher and D. J. Mckenney, *Can. J. Chem.*, 1972, **50**, 2527–2536.

58 D. L. Baulch, J. Duxbury, S. J. Grant and D. C. Montague, *Evaluated Kinetic Data for High Temperature Reactions. Volume 4 Homogeneous Gas Phase Reactions of Halogen- and Cyanide- containing Species*, 1981, vol. 10.

59 P. Roth, M. Y. Louge and R. K. Hanson, *Combust. Flame*, 1986, **64**, 167–176.

60 A. R. Whyte and L. F. Phillips, *Chem. Phys. Lett.*, 1983, **98**, 590–593.

61 B. Brunetti and G. Liuti, *Zeitschrift für Phys. Chemie*, 1975, **94**, 19–30.

62 T. Kruse and P. Roth, *Int. J. Chem. Kinet.*, 1999, **31**, 11–21.

63 D. R. Safrany and W. Jaster, *J. Phys. Chem.*, 1968, **72**, 3305–3318.

64 R. Atkinson, D. L. Baulch, R. A. Cox, R. F. Hampson, J. A. Kerr and J. Troe, *J. Phys. Chem. Ref. Data*, 1989, **18**, 881–1097.

65 Y. He, C. H. Wu, M. C. Lin and C. F. Melius, *The Reaction of CN with NO at High Temperatures in Shock Waves*, Springer, Berlin, Heidelberg, 1995.

66 R. Snoeckx and A. Bogaerts, *Chem. Soc. Rev.*, 2017, **46**, 5805–5863.